Integrative *in vivo* analysis of the ethanolamine utilization bacterial microcompartment in *Escherichia coli*.

Running title: *In vivo* functionality of the *E. coli* Eut BMC

Denis Jallet[1#], Vanessa Soldan[2], Ramteen Shayan[2], Alexandre Stella[3,5], Nour Ismail[1], Rania Zenati[1], Edern Cahoreau[1,4], Odile Burlet-Schiltz[3,5], Stéphanie Balor[2], Pierre Millard[1,4], Stéphanie Heux[1].

[1] Toulouse Biotechnology Institute, Université de Toulouse, CNRS, INRAE, INSA, Toulouse, France

[2] Plateforme de Microscopie Electronique Intégrative, Centre de Biologie Intégrative, Université de Toulouse, CNRS, Toulouse, France

[3] Institut de Pharmacologie et de Biologie Structurale (IPBS), Université de Toulouse, CNRS, Université Toulouse III – Paul Sabatier (UT3), Toulouse, France

[4] MetaToul-MetaboHUB, National infrastructure of metabolomics and fluxomics, Toulouse, France

[5] Infrastructure nationale de protéomique, ProFI, FR 2048, Toulouse, France

Correspondance: denis.jallet@insa-toulouse.fr

Abstract

Bacterial microcompartments (BMCs) are self-assembling protein megacomplexes that encapsulate metabolic pathways. Although approximately 20% of sequenced bacterial genomes contain operons encoding putative BMCs, few have been thoroughly characterized, nor any in the most studied *Escherichia coli* strains. We used an interdisciplinary approach to gain deep molecular and functional insights into the ethanolamine utilization (Eut) BMC system encoded by the *eut* operon in *E. coli* K-12. The *eut* genotype was linked with the ethanolamine utilization phenotype using deletion and overexpression mutants. The subcellular dynamics and morphology of the *E. coli* Eut BMC were characterized *in cellula* by fluorescence microscopy and electron (cryo)microscopy. The minimal proteome reorganization required for ethanolamine utilization and the *in vivo* stochiometric composition of the Eut BMC were determined by quantitative proteomics. Finally, the first flux map connecting the Eut BMC with central metabolism *in cellula* was obtained by genome scale modelling and ^{13}C-fluxomics. Our results reveal that, contrary to previous suggestions, ethanolamine serves both as a nitrogen and a carbon source in *E. coli* K-12, while also contributing significant metabolic overflow. Overall, this study provides a quantitative molecular and functional understanding of the BMCs involved in ethanolamine assimilation by *E. coli*.

Importance

The properties of BMCs make them an ideal tool to build orthogonal network structures with minimal interactions with native metabolic and regulatory networks. However, this requires an understanding of how BMCs work natively. In this study, we combined genetic manipulation, multi-omics, modelling and microscopy to address this issue for Eut BMCs. We show that the Eut BMC in *E. coli* turns ethanolamine into usable carbon and nitrogen substrates to sustain growth. These results improve our understanding of compartmentalization in a widely used bacterial chassis. Potential biotechnological applications include employing native Eut BMCs as tuneable intracellular nano-bioreactors.

Introduction

Compartmentalization was initially considered a defining feature of eukaryotic cells. With the advent of transmission electron microscopy (TEM) however, subcellular structures were also discovered in bacteria, including bacterial microcompartments (BMCs) such as carboxysomes in certain autotrophic taxa[1]. Genes encoding for BMC shell proteins were subsequently discovered in heterotrophic taxa[2] and recent metagenomics data suggest that roughly 20% of bacteria have BMC encoding operons[3]. These genes are generally found in large operons with the other genetic components required to produce BMCs, often referred to as metabolosomes, because of their typically catabolic rather than anabolic function. The ethanolamine utilization (Eut) BMC in *Salmonella enterica* was one of the first studied metabolosome systems[4].

Ethanolamine (EA) accumulates in mammalians' gastrointestinal and urinary tracts upon degradation of phosphatidylethanolamine. Some *Escherichia coli* strains can utilize EA as sole nitrogen and carbon source in the presence of vitamin B12[5–9]. EA utilization was initially thought to be associated with pathogenicity[5,10] but several commensal *E. coli* strains also metabolize EA[8]. The *E. coli* core genome natively hosts a 17-gene *eut* operon (*eutSPQTDMNEJGHABCLKR*) with strong homology to the *eut* operon of *S. enterica*[11,12].

The Eut BMC shell is made up of ring-shaped oligomeric proteins (EutSMNLK), some of which have central pores that allow some small metabolites to pass, including EA and its degradation products[13]. Inside Eut BMCs, EA is thought to be deaminated into acetaldehyde plus ammonium (NH_4) by EAL (EutBC), but the exact metabolic topology involved remains debated[14,15]. Acetaldehyde is further converted through enzymatic reactions. NH_4, ethanol and acetyl-P would eventually diffuse out through the shell to be used in central metabolism or excreted[14]. But again, the exact core protein complement remains hypothetical. Two Eut enzymes (EutC, EutE) bear encapsulation peptides that likely favour their internalization[16,17]. Other Eut enzymes may form complexes or interact with shell components.

Electron micrographs of *E. coli* Eut BMCs have only ever been reported twice[6,18]. Indeed, while irregular polyhedral structures with a diameter of around 100 nm can be observed in *E. coli* K-12 and *E. coli* UPEC U1 after *eut* induction, it is unclear whether these Eut BMCs are well formed and functionally required for EA catabolism. Intact Eut BMCs have never been purified to date, either from *E. coli* or from *S. enterica*, and our knowledge of these systems mainly comes from genetic studies in *S. enterica*[14,15,19] and *in vitro* structural and functional characterizations of individual recombinant Eut proteins[13].

Overall, Eut BMCs play a safeguarding role by sequestering and favouring the downstream conversion of toxic and volatile acetaldehyde intermediates[15]. Their spatial arrangement favours metabolic channelling and it has been reported that compartmentalisation may increase catalytic activity by up to 6-fold compared with non-compartmentalised reactions[20]. Another advantage is that the cofactors required for enzyme activity are regenerated within the BMC thus limiting competition with enzymes from the cytosol[14]. These properties make Eut BMCs and BMCs interesting metabolic units for biotechnological applications[21], but a better understanding of their regulation, assembly and function is still required to make them amenable to engineering.

With these knowledge gaps in mind, we performed a systemic analysis from the molecular to the functional level of native BMC-mediated EA catabolism in *E. coli* K-12. We characterized wild-type (WT) *E. coli* K-12 W3110 and several mutant strains by epifluorescence microscopy, TEM and electron cryotomography (cryoET) and performed a multi omics analysis to understand how BMC-mediated EA utilization affects bacterial physiology.

83 **Results**

84 *1) Necessity of the eut operon for EA utilization.*

85 The *eut* operon of *E. coli* K-12 W3110 (Fig.1A) is similar in gene content to *S. enterica* LT2's, with more
86 than 77 % primary sequence identity between individual Eut proteins from the two species (Table S2).
87 In contrast, the *eut* operon of *E. coli* K-12 BW25113 is natively interrupted by a prophage DNA insertion
88 downstream of *eutA* (Fig.S1A). To investigate the link between *eut* genotype and EA catabolism, we
89 first constructed several mutant strains by genome editing[22]. The *eut* operon was knocked out from
90 WT W3110 to yield W3110 Δ*eut* (Table 1; Fig.S1B). The prophage DNA insertion in BW25113 WT was
91 scarlessly removed to reconstitute an intact *eut* operon, thereby generating BW25113 *eut+*. We
92 additionally built *eut* overexpressors by cloning the entire W3110 WT *eut* operon downstream of an
93 IPTG-inducible promoter (P_{trc}[23]) in pSEVA661[24], yielding pEut (Fig.S1C). pEut was transformed into
94 W3110 Δ*eut* for complementation assays.

95 Growth experiments were performed using a microplate reader to evaluate each strain's EA utilization
96 capacity. The W3110 strains (WT and Δ*eut*) behaved similarly in control M9 medium with glycerol as C
97 source and NH_4Cl as N source (Fig.1B). However, only the WT strain grew in M9 glycerol EA, where EA
98 was the only available N source (Fig.1C). W3110 WT had comparable growth rates (Table 2) but
99 significantly higher OD_{600nm} after 24 h in M9 glycerol EA than in M9 glycerol NH_4Cl (0.73 ± 0.01 VS 0.56
100 ± 0.04). BW25113 WT behaved like W3110 Δ*eut* and BW25113 *eut+* behaved like W3110 WT (Fig.S1D-
101 E), indicating that an uninterrupted *eut* operon is essential for EA utilization as N source. Note that
102 none of the strains grew in M9 EA where EA was the only available N and C source (Fig.S1F). In M9
103 glycerol NH_4Cl with gentamicin (Gm), W3110 Δ*eut* pEut's growth rate was similar to that of the empty-
104 vector control (W3110 Δ*eut* pO) and of the corresponding plasmid-bearing WT derivatives (Table 2;
105 Fig.1B). W3110 Δ*eut* pO did not grow in M9 glycerol EA Gm (Fig.1C) while W3110 Δ*eut* pEut utilized EA
106 as sole N source with a maximal growth rate similar to that of W3110 WT pO (Table 2) but with a
107 markedly lower final OD_{600nm} (0.60 ± 0.01 VS 0.77 ± 0.01). The W3110 *eut* phenotype was thus at least
108 partially recovered in the plasmid construct, even without IPTG induction, which indicates that the P_{trc}
109 promoter is leaky. When 20 µM IPTG was added at culture initiation, W3110 WT pEut and W3110 Δ*eut*
110 pEut had significantly lower growth rates than the empty vector controls in both M9 glycerol NH_4Cl
111 Gm and M9 glycerol EA Gm (Fig.1D,E; Table 2). These results show that *eut* expression levels must be
112 kept low to avoid any negative impact on growth and enable efficient EA utilization.

113 *2) Subcellular localization of the EutC enzyme.*

114 The *eut* operon encodes a functional EA utilization pathway but does it truly drive the production of
115 Eut BMCs *in cellula*? We first attempted to visualize *E. coli* Eut BMCs by fluorescence microscopy and
116 EutC-GFP fusion. We focused on EutC because it natively carries a 20 amino-acid long N-terminal
117 peptide (referred to as $EutC_{1-20}$ hereafter) that should ensure its encapsulation within BMCs[16,17]. To
118 keep expression levels low, the synthetic gene was inserted at the SS9 safe chromosomal locus[25] (Table
119 1; Fig2A) in W3110 WT under the control of an anhydrotetracycline (aTc) inducible promoter ($P_{LtetO-1}$[26]).
120

121 No GFP fluorescence emission was detected in the absence of aTc (Fig.S2A). In M9 glycerol NH_4Cl with
122 8 $ng.ml^{-1}$ aTc, a faint cytosolic GFP signal was observed (Fig.2B). In M9 glycerol EA with 8 $ng.ml^{-1}$ aTc,
123 multiple GFP puncta were observed moving rapidly around the cytosol (Fig.2C; Movie S1). These
124 mobile GFP puncta are similar to those visualized by fluorescence microscopy for the *S. enterica* Eut
125 BMC system[16,27]. There were 5.9 ± 1.1 GFP puncta per bacterium on average, a number that did not
126 vary significantly upon increasing the aTc concentration up to 80 $ng.ml^{-1}$ (6.3 ± 1.2) (Fig.2D,E). To
127 investigate whether $EutC_{1-20}$ alone could drive the encapsulation of a heterologous protein, we also

128 built a smaller cassette expressing the EutC$_{1-20}$-GFP fusion protein (Fig.S2B). W3110 *eutC$_{1-20}$-GFP*
129 behaved like W3110 *eutC-GFP* but with a stronger cytosolic GFP background (Fig.S2C-E), making it
130 harder to distinguish the puncta. The diffuse GFP background in W3110 *eutC$_{1-20}$-GFP* likely came from
131 non-encapsulated EutC$_{1-20}$-GFP fusions.

132 *3) Morphology of Eut BMCs in cellula.*

133 We first used a traditional TEM-based approach to evaluate the integrity of the Eut BMCs *in cellula*. No
134 BMC-like structure was detected in W3110 WT growing in M9 glycerol NH_4Cl (Fig.S3A). In M9 glycerol
135 EA, irregular polyhedral assemblies roughly 100 nm in diameter, with sharp edges and a well-defined
136 delimiting layer were observed in some slices (Fig. S3B). Since these assemblies satisfy the
137 morphological criteria for BMCs[28] we refer to them hereafter as Eut BMCs. These were present in about
138 1 in 50 bacterial slices. On LB medium supplemented with EA and vitamin B12 to induce *eut*, Eut BMCs
139 were detected in about 1 in 10 bacterial slices (Fig.S3C) suggesting that more BMCs were present.
140 Finally, W3110 Δ*eut* pEut was cultivated in LB containing IPTG to strongly induce the *eut* operon
141 expression. Here, BMCs with various polyhedral geometries and dimensions were observed in most
142 bacteria (Fig.S3D). Increasing the *eut* operon expression strength thus increased the number of BMCs
143 per bacterium but had a negative effect on growth.

144 CryoET reconstructions of W3110 WT grown in M9 glycerol EA revealed several cellular features
145 including the inner and outer membranes, ribosomes, and Eut BMCs (Fig.3A-B). Multiple Eut BMCs
146 were observed per bacterium, surrounded by a thin layer (the BMC shell) with sharp edges and vertices
147 (Fig.3C-D). The shell often completely enclosed the core but structures resembling partial Eut BMCs
148 were also present (arrow in Fig.3D). Further experiments are required to determine whether these
149 apparently partial Eut BMCs correspond to (dis)assembling states or are in fact cryoET (e.g. missing
150 wedge) artefacts. The Eut BMC core was somewhat granular in appearance but more electron dense
151 than the surrounding cytoplasm, with several encapsulated components, likely proteins. This was
152 particularly apparent in bacteria with a clear cytosol after partial lysis (Fig.3D). Overall, these *E. coli* Eut
153 BMCs were more heterogenous in size and shape than cyanobacterial carboxysomes[29]. Tomograms of
154 the W3110 Δ*eut* pEut strain cultivated in M9 glycerol EA IPTG as a control showed a higher number of
155 Eut BMCs per bacterium compared with the WT (Fig.3E-F; Fig.S4), but with similar shapes and
156 dimensions. These first ever cryoET images of Eut BMCs in a bacterium demonstrate that native *E. coli*
157 Eut BMCs are properly formed.

158 *4) EA utilization requires minimal reorganization of the proteome.*

159 Since Eut BMCs are protein-based, we investigated how their production affects *E. coli* using label-free
160 quantitative mass spectrometry-based proteomics. Samples were collected and compared between
161 exponentially growing cultures of W3110 WT maintained aerobically in M9 glycerol EA versus M9
162 glycerol NH_4Cl. Of the 1999 quantifiable proteins, only 48 were significantly more abundant and 8 less
163 abundant in M9 glycerol EA compared with M9 glycerol NH_4Cl (Fig.4A; Table S3). Two distinct modules
164 were identified among these proteins by interaction network analysis using STRING v11.5[30] (Fig.4B).

165 Some of the Eut proteins in the first module were detected in M9 glycerol EA only (EutHNPR), while
166 the others were barely detectable in M9 glycerol NH_4Cl and strongly upregulated in M9 glycerol EA,
167 with fold changes ranging from 5 (EutJ) to 325 (EutM) (Fig.4A). This included enzymes linked to EA
168 catabolism (EutAPQDEGBC) and the structural Eut BMC shell components (EutSMNLK). We calculated
169 the abundance of each Eut protein in M9 glycerol EA corrected for the number of theoretically
170 observable tryptic peptides (iBAQ values[31]: Fig.4C), to correct for differences in molecular weight and
171 primary sequences. Relative to the most abundant protein, EutQ, an acetate kinase[32], whose relative
172 abundance was set to 100, the most abundant predicted shell components were EutM, EutL, EutS,

173 EutK and EutN with relative abundances of 96 ± 14, 39 ± 1, 11 ± 3, 8 ± 1, and 1 ± 1, respectively. The
174 most abundant putative Eut BMC core enzymes besides EutQ were EutB, EutE, EutC, EutD, EutG and
175 EutP (a second acetate kinase), with relative abundances of 37 ± 17, 27 ± 10, 24 ± 9, 10 ± 3, 7 ± 1 and
176 7 ± 1, respectively.

177 The second identified module consisted of proteins involved in maintaining intracellular N homeostasis
178 (Fig.4B), a majority of which were more highly expressed in M9 glycerol EA, including the ammonium
179 transporter AmtB, its cognate regulator GlnK and a two-component system (GlnG-GlnL) controlling N
180 assimilation[33,34]. The second module also contained enzymes catalysing (de)amination reactions, such
181 as asparagine synthetase (AsnAB), succinylglutamate semialdehyde dehydrogenase (AstCD), glutamine
182 synthetase (GlnA), and guanine deaminase (GuaD). Proteins involved in the uptake of extracellular
183 dipeptides (DdpAX), polypeptides (OppA) and amino acids (ArgT, CycA, HisQ) were also present.
184 Several regulators and pathways normally mobilized under N starvation conditions were therefore
185 activated in M9 glycerol EA, probably due to the absence of extracellular N sources other than EA. Note
186 that the abundance of cobalamin-independent homocysteine transmethylase (MetE) was 7 times
187 lower in M9 glycerol EA than in M9 glycerol NH_4Cl. MetE normally participates in methionine
188 biosynthesis but it can be replaced by MetH (cobalamin-dependent methionine synthase) in the
189 presence of vitamin B12[35]

190 Overall, these results indicate that the production of Eut BMCs did not have a pleiotropic effect, since
191 only proteins involved in BMC synthesis and N metabolism were affected.

192 *5) Analysis of EA utilization by exometabolomics.*

193 To decipher the metabolic functioning of the Eut BMCs, we grew W3110 WT under aerobic conditions
194 in M9 derivatives containing glycerol as C source and either EA or NH_4Cl as N source (Fig.S5A-B). The
195 cultures reached similar maximal growth rates in both media (Table 3) but the biomass concentration
196 after 12 h was higher with EA than with NH_4Cl (0.97±0.01 $g_{DW}.L^{-1}$ VS 0.72±0.01 $g_{DW}.L^{-1}$).

197 The exometabolome was analysed by ^{1}H-NMR and extracellular uptake and production fluxes were
198 calculated from these data using PhysioFit[36] (Table 3; Fig.S5C-D). With NH_4Cl as sole N source, glycerol
199 was fully assimilated and no by-products were detected. With EA as sole N source, glycerol was
200 consumed at a similar rate and EA was assimilated at a rate of 7.8 ± 0.3 $mmol.g_{DW}^{-1}.h^{-1}$. Ethanol ($q_{P)EtOH}$
201 = 2.6 ± 0.1 $mmol.g_{DW}^{-1}.h^{-1}$) and acetate ($q_{P)Ace}$ = 1.7 ± 0.1 $mmol.g_{DW}^{-1}.h^{-1}$) were excreted, and the acetate
202 was re-consumed upon exhaustion of glycerol and EA, explaining the higher final biomass under this
203 condition. Trace amounts of acetaldehyde were also detected, suggesting that some acetaldehyde
204 leaked from the Eut BMCs and escaped from the cells. Acetate, ethanol and acetaldehyde could all
205 result from EA catabolism[15]. Assuming NADH is recycled within the Eut BMCs, acetate and EtOH should
206 be produced in similar amounts[14]. Since the production rate of EtOH was significantly higher than that
207 of acetate during exponential growth, this suggests either that some of the EA-derived acetate was
208 used by cellular processes or that some of the EtOH was produced within the cytosol.

209 *6) Genome-scale predictions of EA utilization by E. coli.*

210 We next performed flux balance analysis (FBA[37]) on the same data to study the fate of EA in the Eut
211 BMC and cytosol. We adapted the genome scale model (GSM) of *E. coli* iML1515[38] by
212 compartmentalizing EA catabolism inside Eut BMCs, thereby ensuring that NADH and CoA-SH cofactors
213 are recycled within the BMCs, while ATP is recycled in the cytosol (Fig.S6). The model was then
214 constrained with the experimentally measured extracellular fluxes, assuming acetate and EtOH are
215 produced in the BMCs. When maximizing biomass production, the maximal FBA-predicted growth rate
216 was 0.72 h^{-1}. This value is higher than observed experimentally, indicating that glycerol and EA

217 utilization are suboptimal *in vivo*. We therefore constrained the growth rate to the experimental value
218 (Table 3: 0.45 h^{-1}) and defined ATP maintenance as the objective function[39] (Fig.S6). We also carried
219 out flux variability analysis (FVA) to identify the optimal solution and the range of fluxes that each
220 reaction can carry while maintaining at least 99 % of the objective.

221 The model predicted that Eut BMCs produce and release equimolar quantities of acetaldehyde,
222 ethanol, and acetyl-P into the cytosol, each accounting for 33 % of the C from EA (Fig.S6). Acetaldehyde
223 can potentially escape from the cytosol into the extracellular medium, as reported previously[15], and/or
224 be utilized in metabolism. All the ethanol is excreted. Some of the acetyl-P is converted into acetate
225 (21 % of the C from EA) before excretion while the remaining portion can be converted into acetyl-CoA
226 to fuel anabolism and thereby support growth (12 % of the C from EA) (Fig.S6). While EA is thought to
227 act only as a nitrogen source for *E. coli* K-12, genome-scale modelling thus predicts that it may also
228 provide carbon. Moreover, the model indicates that the amount of EA-derived ammonium exceeds
229 the N needs of *E. coli* for growth, and a metabolic steady state can thus only be achieved if some of
230 the ammonium (38 % of the N from EA) is excreted.

231 *7) ^{13}C-metabolic flux analysis of EA and glycerol co-metabolism*

232 To test the predictions of the GSM, we performed a ^{13}C-metabolic flux analysis of W3110 WT grown in
233 M9 medium containing $^{12}C_3$-glycerol and $^{13}C_2$-EA (Fig.5) and quantified the time-course concentrations
234 of labelled and unlabelled EtOH and acetate by ^{1}H-NMR (Fig.5A-B). EtOH was virtually fully labelled
235 (4.66 ± 0.44 mM $^{13}C_2$-EtOH VS 0.47 ± 0.03 mM $^{12}C_2$-EtOH after 10 h, Fig.5B), demonstrating that about
236 90 % was produced from EA. The residual $^{12}C_2$-EtOH may have come either from incomplete
237 encapsulation of Eut enzymes (e.g. EutE converting cysotolic $^{12}C_2$-acetyl-CoA into $^{12}C_2$-acetaldehyde
238 and EutG, yielding $^{12}C_2$-EtOH), from cytosolic acetyl-CoA (produced from unlabelled glycerol) entering
239 misassembled BMCs, or from weak cytosolic conversion of glycerol to ethanol through alternative
240 cytosolic pathways. In contrast, only half of the acetate pool was labelled, indicating that EA and
241 glycerol contributed equally to acetyl-P synthesis and thus to acetate production. The extracellular
242 ammonium concentration, measured by ^{1}H-NMR, increased from 0.4 ± 0.1 mM after 3 h to 4.4 ± 0.1
243 mM after 11 h (Fig.5B).

244 Finally, we built a dynamic isotopic model to quantify *in vivo* fluxes within and around the Eut BMCs
245 by fitting the dynamics of all (labelled and unlabelled) exometabolites (Fig.5C; Table S4). This model
246 includes a coarse-grained representation of glycolytic conversion of glycerol to acetyl-P and of the
247 conversion of acetyl-P into acetate or its utilization elsewhere in metabolism for biomass synthesis, as
248 suggested by the GSM. This model fit the data satisfactorily (Fig.S7), supporting the validity of the
249 assumed network topology. Here, the Eut BMCs released more ethanol (Table S4; v_{EutG} = 2.7 ± 0.1
250 mmol.g_{DW}^{-1}.h^{-1}, 37% of the C from EA) and acetyl-P (v_{EutD} = 2.7 ± 0.1 mmol.g_{DW}^{-1}.h^{-1}, 37% of the C from
251 EA) than acetaldehyde ($v_{BMC)acetaldehyde}$ = 1.7 ± 0.1 mmol.g_{DW}^{-1}.h^{-1}, 26% of the C from EA). Consistent with
252 the labelling data, glycerol and EA contributed equally to the cytosolic acetyl-P pool (with $v_{Glycolysis}$ = 2.5
253 ± 0.1 mmol.g_{DW}^{-1}.h^{-1}). About 32 % of the acetyl-P pool was excreted as acetate ($q_{P)Acetate}$ = 1.6 ± 0.1
254 mmol.g_{DW}^{-1}.h^{-1} ; 12% of the C from EA) and the rest fuelled growth (v_{Pta} = 3.5 ± 0.1 mmol.g_{DW}^{-1}.h^{-1} ; 25%
255 of the C from EA). To confirm the significant anabolic utilization of carbon derived from EA, we
256 measured the carbon isotopologue distributions of proteinogenic amino acids (Fig.5D). In keeping with
257 the high ^{13}C-enrichment of the cytosolic acetyl-P pool (and therefore also the acetyl-CoA pool)
258 predicted by the isotopic model (Fig.S8), amino acids derived from the TCA cycle (i.e. Arg, Glu, Asp,
259 Thr, Lys, Ile) had high fractions of heavy isotopologues. In contrast, amino acids produced from
260 intermediates of the glycolytic and pentose phosphate pathways (i.e. Gly, Ser, His, Tyr, Phe, Ala, Val)
261 had much lower ^{13}C enrichment, pointing to an absence of neoglucogenic flux under the investigated
262 conditions. Carbon derived from EA thus mainly entered central metabolism through the TCA cycle.

263 Regarding N metabolism, the isotopic model confirmed the ammonium overflow predicted by the
264 GSM, with an ammonium production rate of 0.9 ± 0.2 mmol.g_{DW}^{-1}.h^{-1} (Fig.5C; Table S4; 12% of the N
265 from EA). This value is slightly lower than the optimal FBA-predicted value (3.0 mmol.g_{DW}^{-1}.h^{-1}, Fig.S6),
266 possibly because of an underestimation of the quantity of N required to form biomass (which was
267 determined during growth on glucose and ammonia as sole C and N sources, respectively[38]).

268 These isotope labelling experiments thus confirm the main predictions of the genome-scale model,
269 namely that EA can be used as a C source for growth and that N overflow occurs under these
270 conditions.

271 **Discussion**

272 The presence of functional Eut BMCs in *E. coli* has been suggested but never clearly demonstrated.
273 Focusing on the non-pathogenic laboratory strain *E. coli* K-12, our interdisciplinary results provide deep
274 molecular and functional insights into this native Eut BMC system and its importance for EA utilization.

275 We were able to visualize *E. coli* Eut BMCs *in cellula* by TEM and even more clearly by cryoET. The Eut
276 BMCs produced by WT *E. coli* K-12 W3110 were mostly well formed with an electron-dense core
277 separated from the surrounding cytoplasm by a continuous shell layer. Dark particles, presumably Eut
278 enzymes, were present in the core. No array-like particle arrangements were observed, contrary to
279 what has been reported for carboxysomes[29], but similar to observations of the Pdu BMCs of *Acetonema*
280 *longum*[40]. While recent efforts have allowed the internal organisation of α-carboxysomes to be
281 mapped out[41], much less is known of metabolosomes. Working on isolated Eut BMCs would facilitate
282 downstream structural characterisation; however, our attempts to purify *E. coli* Eut BMCs using
283 protocols established for Pdu BMCs[42] or α-carboxysomes[43] failed (data not shown). Apparently, the
284 protein-protein interactions that allow Eut BMCs to assemble and/or persist *in vivo* do not withstand
285 extracellular conditions[44]. Similar difficulties have previously been reported in *S. enterica*[42] and to our
286 knowledge intact Eut BMCs have never been purified from any bacterial species so far, suggesting that
287 Eut BMCs are intrinsically less stable than Pdu BMCs or carboxysomes.

288 We used fluorescence microscopy to observe Eut BMCs *in vivo*. $EutC_{(1-20)}$-GFP formed discrete puncta
289 in M9 glycerol EA only so upon *eut* induction, i.e. when all the other Eut components were present.
290 $EutC_{(1-20)}$-GFP was likely encapsulated inside the Eut BMC core under these conditions. Unlike
291 fluorescently-tagged carboxysomes, which align along the cell axis[45], the $EutC_{(1-20)}$-GFP puncta moved
292 freely around the cytoplasm. This sort of mobility has also been observed for $SeEutC_{1-19}$-EGFP
293 encapsulated in *S. enterica* Eut BMCs *in vivo*[16,27]. Eut BMCs may interact with bacterial cytoskeleton
294 through as-yet undetermined shell-coating proteins, somewhat like Pdu BMCs[46]. However, how Eut
295 BMC subcellular dynamics affect their metabolic functioning or inheritance by daughter cells remains
296 unclear. An EutK-mCherry fusion has recently been used to visualize *Listeria monocytogenes* Eut BMCs
297 *in vivo*[47], which appeared as immobile red puncta. Future work should include the colocalization of
298 core (e.g. EutC) and shell (e.g. EutK) elements to further validate the location of the fluorescent
299 reporters.

300 How many Eut BMCs do *E. coli* K-12 W3110 cells normally contain? Assuming that each GFP punctum
301 corresponded to a single BMC, our data indicate that there were 6 Eut BMCs per bacterium, but this
302 count needs to be confirmed by higher resolution approaches such as correlated light and electron
303 microscopy[48]. In comparison, around 3-4 GFP puncta per bacterium were observed in *S. enterica* after
304 labelling Pdu BMCs with GFP[49]. TEM observations indicate that chemo-autotrophic bacteria contain 3
305 to 80 carboxysomes[29,45]. The number of Eut BMCs likely depends on culture conditions[6]: resource
306 availability and specific regulatory networks (e.g. control by catabolic repression[7]) may modulate

307 expression of the *eut* operon. Even with 5 to 100 BMCs per *E. coli* W3110 WT, Eut BMCs would occupy
308 just 0.2-4 % of the total cytosolic volume.

309 This study also shows that the ability of *E. coli* K-12 to utilize EA as a N source hinges on the *eut* operon,
310 with minor reorganizations of the rest of the proteome. However, expressing *eut* from even a low copy
311 plasmid impaired growth. The underlying physiological cause is most likely the associated metabolic
312 burden because slower growth i) also occurred in a medium containing NH_4Cl as the N source
313 (indicating that the impairment is not simply due to impaired EA catabolism) and ii) was more
314 pronounced after inducing P_{trc} with IPTG. Overexpressing the *eut* operon increased the number of Eut
315 BMCs per bacterium observed by electron microscopy, up to several hundred under certain conditions
316 (e.g. LB IPTG). The same effect (i.e. more Eut BMCs and slower growth) has previously been observed
317 in *Enterococcus faecalis* upon suppressing a negative *eut* regulator[50]. As observed for other
318 proteins[51,52], fine-tuned regulation of the *eut* operon is necessary to achieve the desired metabolic
319 function at a manageable metabolic cost.

320 The protein complement of Eut BMCs remains unclear; however, our relative quantification of *E. coli*
321 Eut proteins *in vivo* can be used to make an educated guess. The most abundant candidate shell
322 component was hexameric (EutM), the second-most was trimeric (EutL) and the most dilute was
323 pentameric (EutN), reminiscent of the Pdu BMC system in *S. enterica*[53]. This is consistent with EutM
324 and EutL forming the facets and edges of the polyhedral shell together with other minor building blocks
325 (i.e. EutS and EutK), and EutN capping the vertices[13]. Among candidate core enzymes, the large (EutB)
326 and small (EutC) subunits of EAL were roughly equimolar, consistent with the holoenzyme's predicted
327 oligomeric state $[(EutB_2EutC_2)_3]$[54]. NADH generating EutE acetaldehyde dehydrogenase was another
328 major putative core component as were Eut enzymes involved in cofactor recycling (EutG for NAD^+ and
329 EutD for CoA-SH).

330 EutQ was found to be highly abundant, ten times more abundant than EutP, the other *eut*-encoded
331 acetate kinase[32]. We think that EutQ and EutP are localized outside the Eut BMC (i.e. on the shell
332 surface or soluble in the cytosol) so that any ATP generated upon EA-derived acetyl-P consumption
333 can feed into cellular metabolism. However, our results do not allow any conclusions to be drawn
334 about the subcellular localizations of EutQ and EutP: either or both enzyme(s) could also be
335 encapsulated within BMCs *in vivo*. EutQ has been reported to interact with EutM *in vitro* and to
336 facilitate the formation of multiple Eut BMCs per bacterium[27]. Since ATP probably cannot transit
337 through the pores in the shell[14], any ATP produced in the core by EutQ and EutP when converting
338 acetyl-P into acetate would have to be recycled internally, e.g. to reactivate EAL after it undergoes
339 catalytic inactivation[55,56].

340 To our knowledge, the flux map reported here is the first to connect the Eut BMC with central
341 metabolism *in cellula*. Our results indicate that *E. coli* Eut BMCs leak non-negligible amounts of
342 acetaldehyde (up to 33 % of the C from EA). In comparison, about 13 and 28 % of the C from 1,2-PD
343 was found to be lost as propionaldehyde by the Pdu BMCs of *Salmonella enterica* [57] and *Propionobacter*
344 *freudenreichii*[58], respectively. Leakage may thus be a common feature of metabolosomes. We did not
345 observe any deleterious effect on growth, suggesting that the concentration of acetaldehyde remained
346 below the toxicity threshold in the cytosol. In our model, the remaining acetaldehyde is converted
347 inside the BMC core into equimolar quantities of ethanol and acetyl-P before diffusing out through
348 shell pores. Some of the EA-derived C then enters central metabolism, mainly through the TCA cycle,
349 to fuel growth. This result is in line with a recent report demonstrating that *E. coli* assimilates acetate
350 (here derived from ethanolamine) with glycolytic substrates when the glycolytic flux is low, such as on
351 glycerol[59], to feed anabolism. But why then is *E. coli* K-12 W3110 WT unable to grow with EA as sole C
352 source? Perhaps the flux of EA assimilation simply did not meet cellular housekeeping demands.

353 Additional comparisons with other *E. coli* strains, including some capable of utilizing EA as sole C
354 source[7,9], are required to identify the underlying mechanisms.

355 By integrating our microscopy and fluxomics data, we calculated the mean EA conversion flux through
356 an individual *E. coli* K-12 Eut BMC *in cellula* (calculations in Supplementary Data 3): the value is close
357 to 0.300 fmol.BMC^{-1}.h^{-1} (or 0.600 fmol C.BMC^{-1}.h^{-1}). This is very close to the mean flux of 1,2-PD
358 conversion through an individual *S. enterica* Pdu BMC *in cellula* (0.350 fmol.BMC^{-1}.h^{-1}, or 1.050 fmol
359 C.BMC^{-1}.h^{-1}) calculated from previous experimental and modelling data[57,60]. The carboxylation rate
360 through an individual carboxysome varies from 0.03 to 4.82 fmol C.BMC^{-1}.h^{-1} depending on
361 conditions[61]. These BMC types seem to operate at similar overall turnover rates, despite having
362 different enzymatic core contents. Although they occupy an almost negligible fraction of the cytosolic
363 volume, our model predicts that Eut BMCs act as efficient nanobioreactors with total C fluxes
364 comparable to those of other major cellular metabolic processes (e.g. a glycolytic flux of 0.72 fmol.cell^{-}
365 ^{1}.h^{-1} or 2.16 fmolC.cell^{-1}.h^{-1} here).

366 Finally, we also found that EA served as a N source, with strong modifications in the levels of proteins
367 involved in nitrogen metabolism. The ammonium generated by EA catabolism was mostly used for
368 biomass production but the rest was excreted. The N:C molar ratio of EA (1:2) is higher than in the
369 elemental composition of *E. coli* (1:4)[62], which explains why our cultures acted as net ammonium
370 producers. Moreover, given that glycerol was the primary C source in M9 glycerol EA, the proportion
371 of excreted ammonium would likely be higher in other media with less organic C (e.g. M9 EA). This may
372 have important physiological implications in the gut microbiome environment. Do EA-utilizing bacteria
373 release ammonium in the gut, making it available for surrounding micro-organisms? EA utilization may
374 influence the composition of complex bacterial communities through C and N overflows.

375 **Conclusion**

376 The native *E. coli* Eut BMC has so far been overlooked by recent efforts to explore the natural diversity
377 of BMC structures and functions. Our interdisciplinary approach shows that the laboratory strain *E. coli*
378 K-12 W3110 produces well-formed Eut BMCs. These Eut BMCs act as orthogonal modules in the
379 cytosol, turning EA into usable N and C substrates for biomass formation, but with significant metabolic
380 overflow. However, some questions remain unanswered as to how the Eut BMCs operate, particularly
381 regarding the subcellular localization of certain Eut proteins (e.g. EutQ) and of cofactor recycling (e.g.
382 ATP). The existence of a native subcellular compartmentalization system shows that *E. coli* has a more
383 complex metabolic organization than originally perceived. This spatial arrangement could be
384 domesticated in the future for synthetic biology applications, with the core Eut BMC content
385 reprogrammed to produce efficient and modular intracellular nanobioreactors. We hope the data from
386 this study will accelerate these developments.

387 **Materials and Methods**

388 <u>Bacterial strains and culture conditions</u>

389 *Media preparation*

390 Cloning experiments were performed in Lysogeny Broth (LB). For the physiological characterizations,
391 a nitrogen-free M9-medium was first assembled containing (final concentration in the medium): 17.4
392 g·L^{-1} $Na_2HPO_4 \cdot 12H_2O$, 3.03 g·L^{-1} KH_2PO4, 0.51 g·L^{-1} NaCl, 0.49 g·L^{-1} MgSO4 and 4.38 mg·L^{-1} $CaCl_2$.
393 Thiamine hydrochloride (100 mg·L^{-1}) was also included, as well as 0.1 % (v/v) of a trace element
394 solution (final concentration in the medium: 15 mg·L^{-1} $Na_2EDTA \cdot 2H_2O$,4.5 mg·L^{-1} $ZnSO_4 \cdot 7H_2O$, 0.3
395 mg·L^{-1} $CoCl_2 \cdot 6H_2O$, 1 mg·L^{-1} $MnCl_2 \cdot 4H_2O$, 1 mg ·L^{-1} H_3BO_3, 0.4 mg·L^{-1} $Na_2MoO \cdot 2H_2O$, 3 mg·L^{-1} FeSO4

396 · $7H_2O$, and 0.3 mg·L^{-1} $CuSO_4 \cdot 5H_2O$). In M9 glycerol ammonium, NH_4Cl (1.07 g·L^{-1} or 20 mM) was added
397 as the nitrogen source and glycerol (2.76 g·L^{-1} or 30 mM) as the organic carbon source. In M9 glycerol
398 EA, NH_4Cl was replaced by ethanolamine (1.22 g·L^{-1} or 20 mM; from a stock solution at 122 g·L^{-1}
399 adjusted to pH 7 with HCl 12 N) and cyanocobalamin was included (200 nM). All media components
400 were autoclaved except for thiamine hydrochloride, the trace element solution, NH_4Cl and
401 ethanolamine that were filter-sterilized instead (Minisart 0.2 mm syringe filter, Sartorius, Germany).
402 Antibiotics were added to both solid and liquid media according to each strain's resistance profile
403 [Ampicillin (Amp) at 100 µg.mL^{-1}, Kanamycin (Km) at 50 µg.mL^{-1}, Spectinomycin (Sp) at 50 µg.mL^{-1}
404 and/or Gentamycin (Gm) at 10 µg.mL^{-1}]. Isopropyl-b-D-thiogalactoside (IPTG) (final concentration 20
405 µM) or anhydrotetracycline (aTc) (final concentration 8ng mL^{-1} or 80 ng mL^{-1}) was also incorporated
406 when indicated. All chemical products were purchased from Sigma-Aldrich (France) unless otherwise
407 specified.

408 *Strains cultivation*

409 *E. coli* K-12 W3110 wild-type (WT) as well as several mutant derivatives were used (Table 1). All the
410 strains were cryopreserved at -80°C in LB with 25 % (w/v) glycerol. The strains were streaked onto LB
411 agar plates and incubated at 37°C for 16 h. An isolated single colony then served to inoculate 2 ml of
412 LB medium before culturing for 8h at 37°C under 200 rpm orbital shaking (Inova 4230, Brunswick
413 Scientific, United States). The optical density at 600 nm (OD_{600nm}) was measured with a Genesys 6
414 spectrophotometer (Thermo Fisher Scientific, United States). The preculture was next diluted into a
415 baffled shake flask (250 ml) containing 50 ml of modified M9-medium, aiming for a starting OD_{600nm} of
416 0.07.

417 After 16h of incubation at 37°C under 200 rpm shaking, the bacteria were collected by centrifugation
418 (4000 × g at room temperature for 3 min) and washed once using modified M9 medium. Finally, the
419 bacteria were inoculated into a baffled flask (250 mL) containing 50 ml of modified M9 medium, again
420 at a starting OD_{600nm} of 0.07. Cultures were performed at 37°C under 200 rpm shaking to proceed with
421 the physiological characterization. The following equation was employed to convert OD_{600nm} values
422 into corresponding biomass dry weight: $g_{DW} = 0.37 \times OD_{600nm}$.

423 When mentioned, cultures were made in a plate format instead. In this case, transparent flat-bottom
424 96 well plates (Sarstedt, Germany) covered with lids and containing 100 µl medium per well were used.
425 The culturing scheme was similar to that described for shake flasks. A CLARIOStar Plus (BMG LabTech,
426 Germany) plate reader apparatus allowed maintaining the cultures at 37°C under 200 rpm double
427 orbital shaking. Absorbance at 600 nm was measured every 10 min to estimate growth. Results were
428 analysed with the MARS Data Analysis software (BMG LabTech, Germany).

429 Molecular biology

430 *Cloning procedures*

431 Polymerase chain reactions (PCRs) for cloning purposes were performed using the high fidelity Phusion
432 DNA Polymerase (NEB, France). PCR products were purified with the NucleoSpin PCR Clean Up kit
433 (Macherey Nagel, Germany), quantified with a NanoDrop 2000 Spectrophotometer (Thermo Fisher
434 Scientific, France) and assembled by In-Fusion (TaKaRa, Japan). After purification with the NucleoSpin
435 Plasmid kit (Macherey Nagel, Germany), the generated plasmids were verified by Sanger Sequencing.

436 *CRISPR-Cas9 genome editing*

437 The system described by Jiang and coworkers was utilized in this study[22]. To generate the Δ*eut* strain,
438 a pTargetF plasmid for *eutG* (pTargetF_eutG) was first constructed. The linear backbone from pTargetF

439 was amplified with primers F_bb1/R_bb1 (see Table S1 for primer sequences). The *eutG* targeting
440 protospacer (PAM shown in bold: CGGCACACCTTCGGTCAATG**CGG**) was amplified with primers
441 F_eutGgRNA/R_eutGgRNA. The generated amplicons were then assembled by In-Fusion to generate
442 pTarget_eutG (Sp^R). Next, the 500 nt situated directly upstream of the P*eut* promoter (upper homology
443 arm) were amplified from purified *E. coli* K-12 W3110 WT gDNA with F_UA1/R_UA1. The same was
444 achieved for the 500 nt downstream of *eutR* (lower homology arm) with F_LA1/R_LA1. The backbone
445 from pUC19 was amplified with F_bb2/R_bb2 and all three fragments were assembled by In-Fusion to
446 yield pHD_Δeut (Amp^R). The linear fragment containing both homology arms was amplified from
447 pHD_Δeut using F_HD1/R_HD1. pTarget_eutG as well as the produced linear fragment were finally
448 electroporated into pCas-containing *E. coli* K-12 W3110 WT bacteria to obtain chromosomally edited
449 Δ*eut* strains. After genotyping, the edited mutants were cured of pTarget_eutG and pCas as described
450 previously.

451 The *SS9* targeting protospacer (TCTGGCGCAGTTGATATGTA**AGG**) was cloned by In-Fusion into pTargetF
452 using primers F_SS9gRNA/R_SS9gRNA and F_bb1/R_bb1, yielding pTargetF_SS9. The 1000 nt upstream
453 of *SS9* were amplified from purified *E. coli* K-12 W3110 WT gDNA with F_UA2/R_UA2, including
454 mutations to suppress the above-mentioned PAM (i.e. AGG to CAA), the 1000 nt downstream of *SS9*
455 with F_LA2/R_LA2. The EutC-GFP and $EutC_{1\text{-}20}$-GFP encoding cassettes ($P_{LtetO\text{-}1}$ promoter, T_{LT0}
456 terminator) were synthesized and cloned with flanking the SS9 homology arms into pUC19, yielding
457 pHD_SS9_eutC-GFP and pHD_SS9_$eutC_{1\text{-}20}$-GFP.

458 *Assembly of pEut_WT.*

459 The linear backbone from pSEVA661_Ptrc (modified version of pSEVA661 bearing a *lacI*^{q} expression
460 cassette and the P_{trc} promoter cloned in its MCS) was amplified with primers F_bb3/R_bb3 (see Table
461 S1). The complete *eut* operon was amplified from isolated *E. coli* K-12 W3110 WT gDNA using
462 F_eut1/R_eut1, F_eut2/R_eut2 as well as F_eut3/R_eut3. The generated amplicons were assembled
463 by In-Fusion to produce the low copy plasmid pEut_WT (Gm^R). Next generation DNA sequencing on an
464 Ion S5 System (Thermo Fisher Scientific, France) was performed at the GeT_Biopuces platform (TBI,
465 INSA Toulouse, France) to verify that the plasmid was properly assembled.

466 Microscopy observations

467 *Epifluorescence microscopy*

468 Samples (equivalent to 0.6 µl culture at OD_{600nm} = 1) were collected after reaching stationary phase
469 and deposited onto GeneFrames (ThermoFisher) containing solidified C-/N-free M9 medium with 1 %
470 agarose. Phase contrast and fluorescence microscopy was performed at room temperature using an
471 automated inverted epifluorescence microscope (Nikon Ti-E/B) equipped with the "perfect focus
472 system" (PFS, Nikon), a phase contrast objective (Plan Apo 100x Oil Ph3 DM NA1.4), a Lumencor
473 SpectraX Light Engine as the illumination source (Ex: 475/34 for GFP), Semrock Brightline multiband
474 dichroic filters (FF409/493/573/652-Di02 for GFP), Semrock emission filters (Em: 536BP40 for GFP) and
475 a Flash4.0 sCMOS camera (Hamamatsu). Fluorescence images were captured and processed using Nis-
476 Elements AR software (Nikon) as well as Fiji[63]. To visualize the mobile fluorescent puncta, pictures were
477 taken every 5 sec over an interval of 30 sec. The puncta were counted manually within n = 30 bacterial
478 cells per samples.

479 *TEM visualization*

480 Samples (equivalent to 1 ml of culture at OD_{600nm} = 1) were collected upon reaching stationary phase
481 by centrifugation at 3000 × g for 3 minutes. Pellets were resuspended in fixation solution (2.5 %

482 glutaraldehyde, 0.1 M cacodylate pH 7.4 as well as 0,04 % w/v ruthenium red) and incubated for 16h
483 at 4°C. Samples were post-fixated in 1 % osmium tetroxide, dehydrated stepwise in ethanol and
484 eventually embedded in the Embed 812 resin (Electron Microscopy Sciences) with a Leica AMW
485 automated device. Thin sections (70 nm width) were stained (solution containing 3 % uranyl acetate
486 in 50 % ethanol as well as Reynold's lead citrate) and observed using a HT 7700 Hitachi transmission
487 electron microscope (accelerating voltage 80 kV, CCD AMT XR41 camera).

488 *cryoET visualization*

489 Samples (equivalent to 1 ml of culture at OD_{600nm} = 1) were collected upon reaching stationary phase
490 and centrifuged at 3000 × g for 3 minutes. Supernatants were discarded. Pellets were washed twice
491 in 1X PBS buffer pH 7.4 and finally resuspended in 50µl of 1X PBS 7.4.

492 Grid preparation: 3.4 µL of sample were deposited onto glow-discharged lacey carbon grids and placed
493 in the thermostatic chamber of a Leica EM-GP automatic plunge freezer, set at 20°C and 95 % humidity.
494 Excess solution was removed by blotting with Whatman n°1 filter paper for 2.5 seconds, and the grids
495 were immediately flash frozen in liquid ethane at -185°C.

496 Cryo-electron tomography: Tilt-series were acquired on a Talos Arctica (Thermo Fisher Scientific)
497 operated at 200 kV in parallel beam condition using either a K2 (for mutant cells) or K3 (for WT
498 condition) Summit direct electron detector and a BioQuantum energy filter (Gatan Inc.) operated in
499 zero-loss mode with a slit width of 20 eV. For WT cells, data collection was carried out using Tomo
500 software (Thermo Fisher Scientific), at a nominal magnification of x31,000 with a calibrated pixel size
501 of 2,78Å. For mutant cells, a nominal magnification of x49000 was used with a calibrated pixel size of
502 2.84Å. In both conditions, tilt series were acquired following the dose symmetric scheme[64] between
503 +50° and −50° with a 2° tilt increment and a defocus range between -10 and -12 µm. Each tilt image
504 was acquired in electron counting mode with cumulative electron dose of 140e-/A² fractionated into
505 ten frames.

506 Tomogram reconstruction and segmentation: Movie frames were aligned using MotionCor2[65] and tilt
507 series were mutually aligned by using 10nm gold particles as fiducial markers and the 3D volumes
508 (tomograms) were reconstructed with weighted back projection using IMOD v.4.11.16[66] software
509 packages with a binning factor of 4. Tomograms were finally denoised and contrast enhanced, boosting
510 the signal to noise ratio (SNR), using Topaz[67] and nonlinear anisotropic diffusion filtering, respectively.
511 Individual objects in tomograms are then segmented using EMAN2 TomoSeg[68], and surfaces of each
512 segmented object are generated and visualized in ChimeraX[69].

513 <u>Proteomics analysis</u>

514 *E. coli* K-12 W3110 WT cultures were grown at 37°C under 200 rpm orbital shaking, in 250 ml flasks
515 containing 50 ml M9 glycerol EA. Upon reaching OD_{600nm} = 1, samples (40 ml) were collected and
516 centrifuged 5 min at 4000 × g. Supernatant was discarded, pellet was resuspended in 3 ml Lysis Buffer
517 [100mM triethylammonium bicarbonate (TEAB) Buffer pH 8,5 with 2,5 % w/v SDS] at 4°C. Bacteria
518 were lyzed by sonication (Fisherbrand sonicator equipped with a microprobe: 20 % power, 20 sec on,
519 30 sec off, cycle repeated twice). After centrifugation 8 min at 13000 × g, supernatant was collected.
520 The protein concentration was determined using a BCA assay.

521 Dried protein extracts (40 µg) were solubilized with 25 µl of 5% SDS. Proteins were submitted to
522 reduction and alkylation of cysteine residues by addition of TCEP and chloroacetamide to a final
523 concentration respectively of 10 mM and 40 mM. Protein samples were then processed for trypsin
524 digestion on S-trap Micro devices (Protifi) according to manufacturer's protocol, with the following

525 modifications: precipitation was performed using 211 µl S-Trap buffer; 4 µg Trypsin was added per
526 sample for digestion, in 25 µl TEAB 50mM pH8.

527 Tryptic peptides were resuspended in 20 µl of 2% acetonitrile and 0.05% trifluoroacetic acid and
528 analyzed by nano-liquid chromatography (LC) coupled to tandem MS, using an UltiMate 3000 system
529 (NCS-3500RS Nano/Cap System; Thermo Fisher Scientific) coupled to an Orbitrap QExactive Plus mass
530 spectrometer (Thermo Fisher Scientific). 5 µl of each sample was loaded on a C18 precolumn (300 µm
531 inner diameter × 5 mm, Thermo Fisher Scientific) in a solvent made of 2% acetonitrile and 0.05%
532 trifluoroacetic acid, at a flow rate of 20 µl/min. After 5 min of desalting, the precolumn was switched
533 online with the analytical C18 column (75 µm inner diameter × 50 cm, in-house packed with Reprosil
534 C18) equilibrated in 95% solvent A (5% acetonitrile, 0.2% formic acid) and 5% solvent B (80%
535 acetonitrile, 0.2% formic acid). Peptides were eluted using a 5%-50% gradient of solvent B over 115
536 min at a flow rate of 300 nl/min. The mass spectrometer was operated in data-dependent acquisition
537 mode with the Xcalibur software. MS survey scans were acquired with a resolution of 70,000 and an
538 AGC target of 3e6. The 10 most intense ions were selected for fragmentation by high-energy collision
539 induced dissociation, and the resulting fragments were analyzed at a resolution of 17500, using an AGC
540 target of 1e5 and a maximum fill time of 50 ms. Dynamic exclusion was used within 30 s to prevent
541 repetitive selection of the same peptide.

542 Raw MS files were processed with the Mascot software (version 2.7.0) for database search and
543 Proline[70] for label-free quantitative analysis (version 2.1.2). Data were searched against *Escherichia coli*
544 entries of the UniProtKB protein database (release Swiss-Prot 2019_11_05, 23,135 entries).
545 Carbamidomethylation of cysteines was set as a fixed modification, whereas oxidation of methionine
546 was set as variable modifications. Specificity of trypsin/P digestion was set for cleavage after K or R,
547 and two missed trypsin cleavage sites were allowed. The mass tolerance was set to 10 ppm for the
548 precursor and to 20 mmu in tandem MS mode. Minimum peptide length was set to 7 amino acids, and
549 identification results were further validated in Proline by the target decoy approach using a reverse
550 database at both a PSM and protein false-discovery rate of 1%. For label-free relative quantification of
551 the proteins across biological replicates and conditions, cross-assignment of peptide ions peaks was
552 enabled inside group with a match time window of 1 min, after alignment of the runs with a tolerance
553 of +/- 600 s.

554 The mass spectrometry proteomics data have been deposited to the ProteomeXchange Consortium
555 via the PRIDE partner repository with the dataset identifier PXD048973.

556 Metabolomics analysis

557 *^{1}H-NMR analysis of culture supernatants*

558 *E. coli* K-12 W3110 WT cultures were grown at 37°C under 200 rpm orbital shaking, in 250 ml flasks
559 containing 50 ml M9 glycerol NH4Cl or EA. For the labelling experiment, fully-labelled ethanolamine
560 ($^{13}C_2$-ethanolamine, InnovaChem, France) was employed in the last culturing step for M9 glycerol EA.
561 Samples (500 µL) were collected every 60 min. Bacteria were immediately removed by filtration
562 (Minisart 0.2 mm syringe filter, Sartorius, Germany) and the flow-through was kept at -20°C until
563 further analysis. The flow-through was thawed and mixed (180 µL) with 20 µL of an internal standard
564 containing 2.35 g/l deuterated trimethylsilylpropanoic acid (TSP-d4) solubilized in D_2O. The ^{1}H-NMR
565 analyses were performed using a quantitative zgpr30 sequence with water pre-saturation prior to
566 acquisition on an Avance III 500-MHz spectrometer. The parameters were as follows: 286 K, 128K
567 points, 4 dummy scans, 64 scans, interscan delay of 8.98 s. Three biological replicates were included
568 for each medium. For the ammonium quantification experiment, the filtration flow through (690 µl,
569 diluted 4X in MQ H2O) was mixed with 7.3 µl 4M H_2SO_4 and 2.7 µl MQ H_2O[71]. TSP-d4 dissolved in D2O

570 (60 µl) was added to 540 µl of the mixture. A solvent suppression proton NMR sequence (zggpw5) at
571 286K with 32K points, 64 scans, 4 dummy scans, and an interscan delay of 10 s was then applied.
572 Quantification was achieved through an external NH_4Cl standard curve (200 mM, 8 mM, 2 mM, 0.5
573 mM and 0.1 mM NH_4Cl diluted in M9 glycerol) analysed with ^{1}H-NMR with the same acquisition
574 parameters and the same sample preparation. Quantification of ammonium in solution was achieved
575 by integration of NMR signals of protons (between 6.9 and 7.4 ppm) attached to nitrogen in an acidic
576 medium, according to the different occurring species (i.e. NH_4, NH_3D, NH_2D_2,) in a mixture of H_2O and
577 D_2O (NHD_3 and ND_4 in negligible amounts were not detected).

578 *Isotopic profiling of proteinogenic amino acids*

579 The same cultures as for NMR analyses were used. Biomass (500µl) was harvested at an OD_{600nm} of 1
580 corresponding to mid-exponential phase. The biomass sample was immediately mixed with 3,5 ml pre-
581 chilled (-20°C) quenching solution made of methanol-acetonitrile-H_2O (4:4:2) containing 125 mM
582 formic acid. The mixture was incubated at -20°C for at least 2 h and then centrifugated at 4500 × g
583 4°C for 5 min. The pellet was stored at -20°C until further usage. After thawing, the pellet was
584 evaporated to dryness with an Orbitrap apparatus (Thermo Fisher Scientific, USA) and hydrolyzed for
585 16h at 105°C with 500 µL HCl 6N. Samples were washed twice before being resuspended into 250 µL
586 ultrapure water and diluted (1:700) for the mass spectrometry analysis. LC-MS was performed on an
587 Ultimate 3000 HPLC system (Dionex, CA, USA) coupled to an LTQ Orbitrap Velos mass spectrometer
588 (Thermo Fisher Scientific, USA). Full scan HRMS analyses were performed in positive FTMS mode, the
589 acquisition parameters and data analysis pipeline being identical to that previously described by
590 Heuillet and coworkers[72]. IsoCor[73] allowed correcting for natural isotopic abundances to determine the
591 carbon isotopologue distributions (CIDs).

592 Modelling

593 *Extracellular uptake and production fluxes*

594 Glycerol and ethanolamine uptake fluxes, acetate and ethanol production fluxes, and growth rates
595 were calculated from glycerol, ethanolamine, acetate, ethanol, and biomass concentration−time
596 profiles using PhysioFit (v1.0.1[36], https://github.com/MetaSys-LISBP/PhysioFit). Ethanol evaporation
597 was considered when calculating ethanol production flux, as detailed in Peiro et al.[74] using an
598 evaporation constant of 0.0379 h^{-1} that was determined experimentally.

599 *Genome-scale modelling of glycerol and ethanolamine co-metabolism.*

600 The iML1515 *E. coli* genome scale model[38] was first updated by incorporating the EA assimilation
601 reactions catalysed by Eut enzymes (EutBC, EutG, EutE, EutD as well as EutQ/P) and the Eut BMC
602 subcellular compartment. We assumed that EutBC, EutG, EutE and EutD were all encapsulated within
603 the Eut BMC core as suggested previously[15], while EutQ/P were assumed to be cytosolic. We also
604 assumed cofactors (i.e. NAD(H) and CoA-SH) to not exchange between the eut BMC and the cytosol,
605 thus being recycled internally within the Eut BMC core. We finally assumed that acetate and ethanol
606 originated from the Eut BMCs. Flux balance analyses and flux variability analyses were carried out using
607 *cobrapy*[75] after constraining exchange fluxes with experimental uptake fluxes of *E. coli* K-12 W3110 WT
608 (see results). The final model iDJ1518 and the scripts used to perform the calculations can be found at
609 https://github.com/MetaSys-LISBP/ethanolamine_metabolism. The genome-scale model is also
610 available from the BioModels database[76] (http://www.ebi.ac.uk/biomodels) with identifier
611 MODEL2403010003.

612 *^{13}C-metabolic flux analysis.*

To quantify intracellular fluxes during growth of *E. coli* on glycerol and ethanolamine, we constructed a dynamic ^{13}C-flux model following the approach detailed before[77] . The model contains 21 reactions, 20 species, and 3 compartments (the environment, the cytoplasm and the eut BMCs), and represents five processes: i) growth, ii) glycerol uptake and conversion into acetyl-phosphate (AcP) by glycolysis, iii) ethanolamine assimilation and conversion through the eut BMCs, iv) AcP utilization by the TCA cycle, v) acetate, acetaldehyde, ethanol and ammonia excretion (Figure 5).

The differential equations, which balance the concentrations of extracellular compounds (biomass, glycerol, ethanolamine, acetate and ethanol) and intracellular compounds (AcP, AcCoA, ethanolamine, ethanol, acetate, glycerol, NAD(H) and ammonia), were completed with isotopic equations for parameter estimation. As detailed before[78], we considered all reactions (except biomass synthesis) separately for unlabeled and labelled reactants. Fluxes were assumed to be constant over time since the cells were assumed to be at metabolic steady-state during exponential growth phase. We also took ethanol evaporation into account, which was modeled with a mass action rate law, using the evaporation constant determined experimentally in this study. The final model has 13 free parameters in total. These parameters (p) were estimated by fitting to the experimentally determined concentration dynamics of biomass, glycerol, ethanolamine, ethanol and unlabeled and labelled acetate, by minimizing the objective function f defined as the weighted sum of squared errors:

$f(p) = \sum_i \left(\frac{x_i - y_i(p)}{\sigma_i}\right)^2$ where x_i is the experimental value of data point i, with an experimental standard deviation σ_i, and $y_i(p)$ is the corresponding simulated value. The objective function f was minimised using the particle swarm optimisation algorithm (2,000 iterations with a swarm size of 50). The experimental and fitted data of one biological replicate are shown in Figure 5, and detailed results for all replicates are provided in Supplementary Figure 7 and Supplementary Data 2.

The model was constructed and analysed using COPASI[79] (v4.27) and is provided in SBML and COPASI formats in the Supplementary data 2 and at https://github.com/MetaSys-LISBP/ethanolamine_metabolism. The model has also been deposited in the Biomodels database (https://www.ebi.ac.uk/biomodels)[76] with the identifier MODEL2403010002 to ensure reproducibility and reusability. Extensive details on the model are provided in Supplementary Data 2.

Calculation of the flux through individual BMCs

All the detailed calculations are given in Supplementary Data 3.

Acknowledgements:

We thank Isabelle Fourquaux (CMEAB) and Sylvain Cantaloube (CBI-LITC) for their technical help. This work was funded by grants from INRAe (NANOBEs and ColiMATTERS projects) and by the ANR (FUNCEMM, ANR-23-CE44-0038). The work was also funded in part by grants from the Région Occitanie, European funds (Fonds Européens de Développement Régional, FEDER), Toulouse Métropole, and the French Ministry of Research with the Investissement d'Avenir Infrastructures Nationales en Biologie et Santé program (ProFI, Proteomics French Infrastructure project, ANR-10-INBS-08). We acknowledge the METi imaging facility, member of the national infrastructure France-BioImaging supported by the French National Research Agency (ANR-10-INBS-04).

Bibliography:

1. Shively, J. M., Decker, G. L. & Greenawalt, J. W. Comparative ultrastructure of the thiobacilli. *J. Bacteriol.* **101**, 618–627 (1970).

655 2. Chen, P., Andersson, D. I. & Roth, J. R. The control region of the pdu/cob regulon in Salmonella
656 typhimurium. *J. Bacteriol.* **176**, 5474–5482 (1994).

657 3. Sutter, M., Melnicki, M. R., Schulz, F., Woyke, T. & Kerfeld, C. A. A catalog of the diversity and
658 ubiquity of bacterial microcompartments. *Nat. Commun.* **12**, 1–12 (2021).

659 4. Stojiljkovic, I., Bäumler, A. J. & Heffron, F. Ethanolamine utilization in Salmonella typhimurium:
660 nucleotide sequence, protein expression, and mutational analysis of the cchA cchB eutE eutJ
661 eutG eutH gene cluster. *J. Bacteriol.* **177**, 1357–1366 (1995).

662 5. Bertin, Y. *et al.* Enterohaemorrhagic Escherichia coli gains a competitive advantage by using
663 ethanolamine as a nitrogen source in the bovine intestinal content. *Environ. Microbiol.* **13**, 365–
664 377 (2011).

665 6. Dadswell, K. *et al.* Bacterial microcompartment-mediated ethanolamine metabolism in
666 Escherichia coli urinary tract infection. *Infect. Immun.* **87**, e00211-19 (2019).

667 7. Jones, P. W. & Turner, J. M. Interrelationships between the enzymes of ethanolamine
668 metabolism in Escherichia coli. *Microbiology* **130**, 299–308 (1984).

669 8. Rowley, C. A., Anderson, C. J. & Kendall, M. M. Ethanolamine influences human commensal
670 Escherichia coli growth, gene expression, and competition with enterohemorrhagic E. coli
671 O157: H7. *MBio* **9**, e01429-18 (2018).

672 9. de Gouveia, M. I. M., Daniel, J., Garrivier, A., Bernalier-Donadille, A. & Jubelin, G. Diversity of
673 ethanolamine utilization by human commensal Escherichia coli. *Res. Microbiol.* **174**, 103989
674 (2023).

675 10. Kendall, M. M., Gruber, C. C., Parker, C. T. & Sperandio, V. Ethanolamine controls expression of
676 genes encoding components involved in interkingdom signaling and virulence in
677 enterohemorrhagic Escherichia coli O157: H7. *MBio* **3**, e00050-12 (2012).

678 11. Tsoy, O., Ravcheev, D. & Mushegian, A. Comparative genomics of ethanolamine utilization. *J.*
679 *Bacteriol.* **191**, 7157–7164 (2009).

680 12. Stewart, K. L., Stewart, A. M. & Bobik, T. A. Prokaryotic organelles: bacterial
681 microcompartments in E. coli and Salmonella. *EcoSal Plus* **9**, (2020).

682 13. Tanaka, S., Sawaya, M. R. & Yeates, T. O. Structure and mechanisms of a protein-based
683 organelle in Escherichia coli. *Science (80-.).* **327**, 81–84 (2010).

684 14. Huseby, D. L. & Roth, J. R. Evidence that a metabolic microcompartment contains and recycles
685 private cofactor pools. *J. Bacteriol.* **195**, 2864–2879 (2013).

686 15. Penrod, J. T. & Roth, J. R. Conserving a volatile metabolite: a role for carboxysome-like
687 organelles in Salmonella enterica. *J. Bacteriol.* **188**, 2865–2874 (2006).

688 16. Choudhary, S., Quin, M. B., Sanders, M. A., Johnson, E. T. & Schmidt-Dannert, C. Engineered
689 protein nano-compartments for targeted enzyme localization. *PLoS One* **7**, e33342 (2012).

690 17. Jakobson, C. M., Kim, E. Y., Slininger, M. F., Chien, A. & Tullman-Ercek, D. Localization of proteins
691 to the 1, 2-propanediol utilization microcompartment by non-native signal sequences is
692 mediated by a common hydrophobic motif. *J. Biol. Chem.* **290**, 24519–24533 (2015).

693 18. Shively, J. M. *et al.* Sequence homologs of the carboxysomal polypeptide CsoS1 of the thiobacilli
694 are present in cyanobacteria and enteric bacteria that form carboxysomes-polyhedral bodies.
695 *Can. J. Bot.* **76**, 906–916 (1998).

696 19. Brinsmade, S. R., Paldon, T. & Escalante-Semerena, J. C. Minimal functions and physiological

697 conditions required for growth of Salmonella enterica on ethanolamine in the absence of the
698 metabolosome. *J. Bacteriol.* **187**, 8039–8046 (2005).

699 20. Chessher, A., Breitling, R. & Takano, E. Bacterial microcompartments: biomaterials for synthetic
700 biology-based compartmentalization strategies. *ACS Biomater. Sci. Eng.* **1**, 345–351 (2015).

701 21. Held, M., Quin, M. B. & Schmidt-Dannert, C. Eut bacterial microcompartments: insights into
702 their function, structure, and bioengineering applications. *Microb. Physiol.* **23**, 308–320 (2013).

703 22. Jiang, Y. *et al.* Multigene editing in the Escherichia coli genome via the CRISPR-Cas9 system.
704 *Appl. Environ. Microbiol.* **81**, 2506–2514 (2015).

705 23. Amann, E., Ochs, B. & Abel, K.-J. Tightly regulated tac promoter vectors useful for the expression
706 of unfused and fused proteins in Escherichia coli. *Gene* **69**, 301–315 (1988).

707 24. Silva-Rocha, R. *et al.* The Standard European Vector Architecture (SEVA): a coherent platform
708 for the analysis and deployment of complex prokaryotic phenotypes. *Nucleic Acids Res.* **41**,
709 D666–D675 (2013).

710 25. Bassalo, M. C. *et al.* Rapid and efficient one-step metabolic pathway integration in E. coli. *ACS*
711 *Synth. Biol.* **5**, 561–568 (2016).

712 26. Lutz, R. & Bujard, H. Independent and tight regulation of transcriptional units in Escherichia coli
713 via the LacR/O, the TetR/O and AraC/I1-I2 regulatory elements. *Nucleic Acids Res.* **25**, 1203–
714 1210 (1997).

715 27. Held, M. *et al.* Engineering formation of multiple recombinant Eut protein nanocompartments
716 in E. coli. *Sci. Rep.* **6**, 24359 (2016).

717 28. Lee, M. J., Palmer, D. J. & Warren, M. J. Biotechnological advances in bacterial
718 microcompartment technology. *Trends Biotechnol.* **37**, 325–336 (2019).

719 29. Iancu, C. V *et al.* Organization, structure, and assembly of α-carboxysomes determined by
720 electron cryotomography of intact cells. *J. Mol. Biol.* **396**, 105–117 (2010).

721 30. Szklarczyk, D. *et al.* STRING v11: protein–protein association networks with increased coverage,
722 supporting functional discovery in genome-wide experimental datasets. *Nucleic Acids Res.* **47**,
723 D607–D613 (2019).

724 31. Schwanhäusser, B. *et al.* Global quantification of mammalian gene expression control. *Nature*
725 **473**, 337–342 (2011).

726 32. Moore, T. C. & Escalante-Semerena, J. C. The EutQ and EutP proteins are novel acetate kinases
727 involved in ethanolamine catabolism: physiological implications for the function of the
728 ethanolamine metabolosome in S almonella enterica. *Mol. Microbiol.* **99**, 497–511 (2016).

729 33. Javelle, A., Severi, E., Thornton, J. & Merrick, M. Ammonium sensing in Escherichia coli: role of
730 the ammonium transporter AmtB and AmtB-GlnK complex formation. *J. Biol. Chem.* **279**, 8530–
731 8538 (2004).

732 34. van Heeswijk, W. C., Westerhoff, H. V & Boogerd, F. C. Nitrogen assimilation in Escherichia coli:
733 putting molecular data into a systems perspective. *Microbiol. Mol. Biol. Rev.* **77**, 628–695
734 (2013).

735 35. Weissbach, H. & Brot, N. Regulation of methionine synthesis in Escherichia coli. *Mol. Microbiol.*
736 **5**, 1593–1597 (1991).

737 36. Le Gregam, L. *et al.* PhysioFit: a software to quantify cell growth parameters and extracellular
738 fluxes. *bioRxiv* 2010–2023 (2023).

739 37. Orth, J. D., Thiele, I. & Palsson, B. Ø. What is flux balance analysis? *Nat. Biotechnol.* **28**, 245–248
740 (2010).

741 38. Monk, J. M. *et al.* i ML1515, a knowledgebase that computes Escherichia coli traits. *Nat.*
742 *Biotechnol.* **35**, 904–908 (2017).

743 39. Schuetz, R., Kuepfer, L. & Sauer, U. Systematic evaluation of objective functions for predicting
744 intracellular fluxes in Escherichia coli. *Mol. Syst. Biol.* **3**, 119 (2007).

745 40. Tocheva, E. I. *et al.* Structure and expression of propanediol utilization microcompartments in
746 Acetonema longum. *J. Bacteriol.* **196**, 1651–1658 (2014).

747 41. Evans, S. L. *et al.* Single-particle cryo-EM analysis of the shell architecture and internal
748 organization of an intact α-carboxysome. *Structure* **31**, 677–688 (2023).

749 42. Sturms, R., Streauslin, N. A., Cheng, S. & Bobik, T. A. In Salmonella enterica, ethanolamine
750 utilization is repressed by 1, 2-propanediol to prevent detrimental mixing of components of two
751 different bacterial microcompartments. *J. Bacteriol.* **197**, 2412–2421 (2015).

752 43. Fang, Y. *et al.* Engineering and modulating functional cyanobacterial CO2-fixing organelles.
753 *Front. Plant Sci.* **9**, 739 (2018).

754 44. Cheng, S., Liu, Y., Crowley, C. S., Yeates, T. O. & Bobik, T. A. Bacterial microcompartments: their
755 properties and paradoxes. *Bioessays* **30**, 1084–1095 (2008).

756 45. Savage, D. F., Afonso, B., Chen, A. H. & Silver, P. A. Spatially ordered dynamics of the bacterial
757 carbon fixation machinery. *Science (80-.).* **327**, 1258–1261 (2010).

758 46. Parsons, J. B. *et al.* Synthesis of empty bacterial microcompartments, directed organelle protein
759 incorporation, and evidence of filament-associated organelle movement. *Mol. Cell* **38**, 305–315
760 (2010).

761 47. Chatterjee, A., Kaval, K. G. & Garsin, D. A. Role of Ethanolamine Utilization and Bacterial
762 Microcompartment Formation in Listeria monocytogenes Intracellular Infection. *bioRxiv* 2012–
763 2023 (2023).

764 48. Hoffman, D. P. *et al.* Correlative three-dimensional super-resolution and block-face electron
765 microscopy of whole vitreously frozen cells. *Science (80-.).* **367**, eaaz5357 (2020).

766 49. Kennedy, N. W. *et al.* Linking the Salmonella enterica 1, 2-propanediol utilization bacterial
767 microcompartment shell to the enzymatic core via the shell protein PduB. *J. Bacteriol.* **204**,
768 e00576-21 (2022).

769 50. Kaval, K. G. *et al.* Ethanolamine utilization and bacterial microcompartment formation are
770 subject to carbon catabolite repression. *J. Bacteriol.* **201**, e00703-18 (2019).

771 51. Glick, B. R. Metabolic load and heterologous gene expression. *Biotechnol. Adv.* **13**, 247–261
772 (1995).

773 52. Ceroni, F. *et al.* Burden-driven feedback control of gene expression. *Nat. Methods* **15**, 387–393
774 (2018).

775 53. Yang, M. *et al.* Decoding the stoichiometric composition and organisation of bacterial
776 metabolosomes. *Nat. Commun.* **11**, 1976 (2020).

777 54. Shibata, N. *et al.* Crystal structures of ethanolamine ammonia-lyase complexed with coenzyme
778 B12 analogs and substrates. *J. Biol. Chem.* **285**, 26484–26493 (2010).

779 55. Mori, K., Bando, R., Hieda, N. & Toraya, T. Identification of a reactivating factor for

780 adenosylcobalamin-dependent ethanolamine ammonia lyase. *J. Bacteriol.* **186**, 6845–6854
781 (2004).

782 56. Costa, F. G. & Escalante-Semerena, J. C. Localization and interaction studies of the Salmonella
783 enterica ethanolamine ammonia-lyase (EutBC), its reactivase (EutA), and the EutT corrinoid
784 adenosyltransferase. *Mol. Microbiol.* **118**, 191–207 (2022).

785 57. Sampson, E. M. & Bobik, T. A. Microcompartments for B12-dependent 1, 2-propanediol
786 degradation provide protection from DNA and cellular damage by a reactive metabolic
787 intermediate. *J. Bacteriol.* **190**, 2966–2971 (2008).

788 58. Dank, A. *et al.* Bacterial microcompartment-dependent 1, 2-propanediol utilization of
789 Propionibacterium freudenreichii. *Front. Microbiol.* **12**, 679827 (2021).

790 59. Millard, P., Gosselin-Monplaisir, T., Uttenweiler-Joseph, S. & Enjalbert, B. Acetate is a beneficial
791 nutrient for E. coli at low glycolytic flux. *EMBO J.* e113079 (2023).

792 60. Jakobson, C. M., Tullman-Ercek, D., Slininger, M. F. & Mangan, N. M. A systems-level model
793 reveals that 1, 2-Propanediol utilization microcompartments enhance pathway flux through
794 intermediate sequestration. *PLoS Comput. Biol.* **13**, e1005525 (2017).

795 61. Mangan, N. M. & Brenner, M. P. Systems analysis of the CO2 concentrating mechanism in
796 cyanobacteria. *Elife* **3**, e02043 (2014).

797 62. Heldal, M., Norland, S. & Tumyr, O. X-ray microanalytic method for measurement of dry matter
798 and elemental content of individual bacteria. *Appl. Environ. Microbiol.* **50**, 1251–1257 (1985).

799 63. Schindelin, J. *et al.* Fiji: an open-source platform for biological-image analysis. *Nat. Methods* **9**,
800 676–682 (2012).

801 64. Hagen, W. J. H., Wan, W. & Briggs, J. A. G. Implementation of a cryo-electron tomography tilt-
802 scheme optimized for high resolution subtomogram averaging. *J. Struct. Biol.* **197**, 191–198
803 (2017).

804 65. Mastronarde, D. N. Automated electron microscope tomography using robust prediction of
805 specimen movements. *J. Struct. Biol.* **152**, 36–51 (2005).

806 66. Kremer, J. R., Mastronarde, D. N. & McIntosh, J. R. Computer visualization of three-dimensional
807 image data using IMOD. *J. Struct. Biol.* **116**, 71–76 (1996).

808 67. Bepler, T., Kelley, K., Noble, A. J. & Berger, B. Topaz-Denoise: general deep denoising models
809 for cryoEM and cryoET. *Nat. Commun.* **11**, 5208 (2020).

810 68. Chen, M. *et al.* A complete data processing workflow for cryo-ET and subtomogram averaging.
811 *Nat. Methods* **16**, 1161–1168 (2019).

812 69. Pettersen, E. F. *et al.* UCSF ChimeraX: Structure visualization for researchers, educators, and
813 developers. *Protein Sci.* **30**, 70–82 (2021).

814 70. Bouyssié, D. *et al.* Proline: an efficient and user-friendly software suite for large-scale
815 proteomics. *Bioinformatics* **36**, 3148–3155 (2020).

816 71. Hodgetts, R. Y. *et al.* Refining universal procedures for ammonium quantification via rapid 1H
817 NMR analysis for dinitrogen reduction studies. *ACS Energy Lett.* **5**, 736–741 (2020).

818 72. Heuillet, M. *et al.* Methodology for the validation of isotopic analyses by mass spectrometry in
819 stable-isotope labeling experiments. *Anal. Chem.* **90**, 1852–1860 (2018).

820 73. Millard, P., Letisse, F., Sokol, S. & Portais, J.-C. IsoCor: correcting MS data in isotope labeling

821 experiments. *Bioinformatics* **28**, 1294–1296 (2012).

822 74. Peiro, C. *et al.* Chemical and metabolic controls on dihydroxyacetone metabolism lead to
823 suboptimal growth of Escherichia coli. *Appl. Environ. Microbiol.* **85**, e00768-19 (2019).

824 75. Ebrahim, A., Lerman, J. A., Palsson, B. O. & Hyduke, D. R. COBRApy: constraints-based
825 reconstruction and analysis for python. *BMC Syst. Biol.* **7**, 1–6 (2013).

826 76. Malik-Sheriff, R. S. *et al.* BioModels—15 years of sharing computational models in life science.
827 *Nucleic Acids Res.* **48**, D407–D415 (2020).

828 77. Millard, P., Enjalbert, B., Uttenweiler-Joseph, S., Portais, J.-C. & Létisse, F. Control and
829 regulation of acetate overflow in Escherichia coli. *Elife* **10**, e63661 (2021).

830 78. Millard, P., Portais, J.-C. & Mendes, P. Impact of kinetic isotope effects in isotopic studies of
831 metabolic systems. *BMC Syst. Biol.* **9**, 1–13 (2015).

832 79. Hoops, S. *et al.* COPASI—a complex pathway simulator. *Bioinformatics* **22**, 3067–3074 (2006).

833

Strains or plasmids	Genotype or description	Source
***E. coli* bacterial strains**		
W3110 WT	*E. coli* K-12 W3110 wild-type [F^- λ^- INV(*rrnD-rrnE*) *rph-1 eut*$^+$]	Laboratory collection
BW25113 WT	*E. coli* K-12 W3110 wild-type [F^- λ^- Δ*lacZ4787*(::*rrnB-3*) *hsdR514* Δ*(araBAD)567* Δ*(rhaBAD)568 rph-1 eut*$^-$(*:: cryptic prophage DNA*)]	Laboratory collection
W3110 Δ*eut*	Chromosomal *eut* operon removed by genome editing in W3110 WT	This study
BW25113 *eut*+	Cryptic prophage DNA insertion within the chromosomal *eut* operon removed by genome editing in BW25113 WT	This study
W3110 *eutC-GFP*	$P_{LtetO-1}$::*eutC-GFP* construct inserted at the SS9 safe chromosomal site in W3110 WT by genome editing	This study
W3110 *eutC*$_{1-20}$-*GFP*	$P_{LtetO-1}$::*eutC*$_{1-20}$-*GFP* construct inserted at the SS9 safe chromosomal site in W3110 WT by genome editing	This study
Plasmids		
pCas	*repA101*(Ts), *Kan*^{R}, P_{cas}::*cas9* P_{araB}::*Red lacIq* P_{trc}::*sgRNA-pMB1*	[22]
pTargetF	*pMB1*, *Sp*^{R}, *sgRNA-acs*; expression of a specific sgRNA to target *acs* in *E. coli*	[22]
pTargetF_eut	*pMB1*, Sp^R, sgRNA-*eutG*; pTargetF derivative for the expression of a specific sgRNA to target *eutG* in *E. coli*	This study
pHD_Δ*eut*	*pUC*, Amp^R, contains the 1kb-long upper and lower homology arms required to knock out the chromosomal *eut* operon in W3110 WT	This study
pTargetF_SS9	*pMB1*, Sp^R, sgRNA-*SS9*; pTargetF derivative for the expression of a specific sgRNA to target the *SS9* locus in *E. coli*	This study
pHD_SS9_eutC-GFP	*pUC*, Amp^R, contains 1kb-long homology regions to insert the $P_{LtetO-1}$::*eutC-GFP* construct at the SS9 safe chromosomal site in W3110 WT	This study
pHD_SS9_eutC$_{1-20}$-GFP	*pUC*, Amp^R, contains 1kb-long homology regions to insert the $P_{LtetO-1}$::*eutC*$_{1-20}$-*GFP* construct at the SS9 safe chromosomal site in W3110 WT	This study
pSEVA661	*p15A*, Gm^R	[24]
pO	*lacI*$_Q$-P_{trc} cassette and T_0 terminator cloned into the multiple cloning site of pSEVA 661	This study
pEut	Entire *eut* operon from W3110 WT cloned into pO under control of P_{trc}	This study

Table 1. Bacterial strains and plasmids used in the study.

	μ_{max} (h^{-1})			
Strain/Medium	**M9 glycerol NH_4Cl**	**M9 glycerol NH_4Cl IPTG**	**M9 glycerol EA**	**M9 glycerol EA IPTG**
WT	0,37 ± 0,01	0,37 ± 0,01	0,39 ± 0,01	0,39 ± 0,01
Δ*eut*	0,36 ± 0,03	0,35 ± 0,01	0,09 ± 0,06	0,03 ± 0,02
WT pO	0,35 ± 0,01	0,36 ± 0,01	0,38 ± 0,03	0,35 ± 0,01
WT pEut	0,33 ± 0,01	0,19 ± 0,01	0,37 ± 0,01	0,23 ± 0,01
Δeut pO	0,35 ± 0,01	0,35 ± 0,01	0,12 ± 0,11	0,02 ± 0,01
Δ*eut* pEut	0,33 ± 0,01	0,19 ± 0,01	0,37 ± 0,01	0,25 ± 0,01

Table 2. Growth of *E. coli* K-12 W3110 strains grown in various M9 medium derivatives. These experiments were performed using a microplate reader. Data are shown as mean (n = 3 biological replicates) ± standard deviation.

	Physiological parameters				
Medium	**μ**	**$q_{S)glycerol}$**	**$q_{S)Ethanolamine}$**	**$q_{P)acetate}$**	**$q_{P)ethanol}$**
M9 gly NH_4Cl	0.44 ± 0.02	16.2 ± 1.6	ND	ND	ND
M9 gly EA	0.45 ± 0.01	14.7 ± 0.4	7.8 ± 0.3	1.7 ± 0.1	2.6 ± 0.1

Table 3. Growth parameters of *E. coli* K12 W3110 WT grown aerobically in M9 medium containing glycerol as C source and NH_4Cl or EA as N source. The exponential growth rate μ is expressed in h^{-1}; the substrate uptake (q_S) and product formation (q_P) rates are expressed in mmol.(gDW.h)$^{-1}$. DW: dry weight; ND: not detected. Data are shown as mean (n = 3 biological replicates) ± standard deviation.

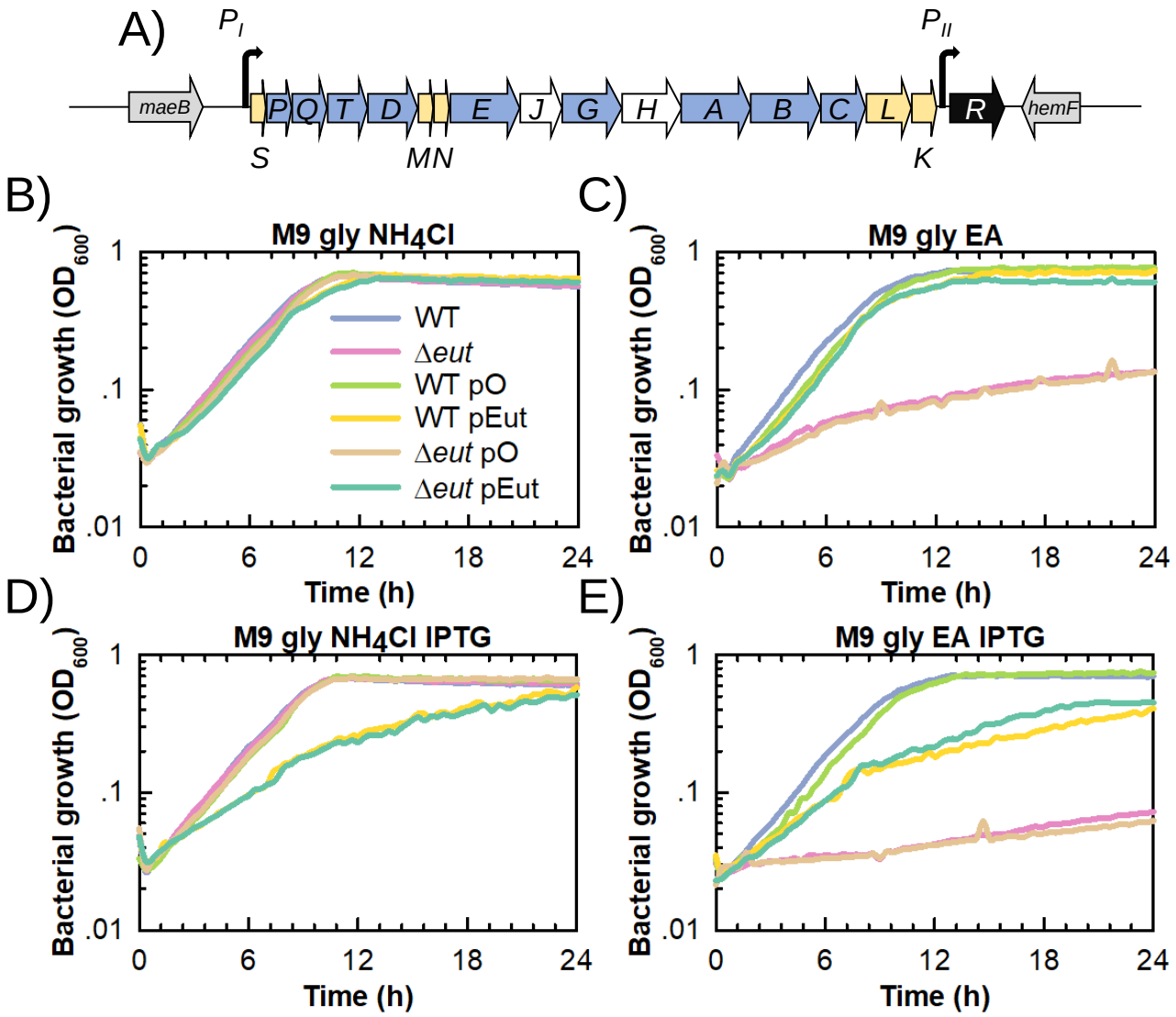

Figure 1. The *eut* operon is essential for EA utilization as nitrogen source by *E. coli* K-12 W3110. A) Schematic representation of the chromosomal *eut* locus in W3110 WT. Genes colored in yellow encode structural components of the Eut BMC shell, those in blue code for enzymes (EA catabolism, coenzyme B12 biosynthesis) and those in white encode other functions (chaperon, transporter). B) to E) Plate reader measurements of optical density at 600 nm for strains grown in B) M9 medium containing glycerol (30 mM) as C source and NH_4Cl (20 mM) as N source; C) M9 medium containing glycerol (30 mM) as C source and EA (20 mM) as N source, including vitamin B12 (200 nM); D) M9 glycerol NH_4Cl with IPTG (20 µM) and E) M9 glycerol EA vitamin B12 with IPTG (20 µM). All the strains and plasmids are described in Table 1. Gentamicin (10 $\mu g.mL^{-1}$) was added for the plasmid-bearing strains. The data shown are from a representative experiment of at least three independent replicates.

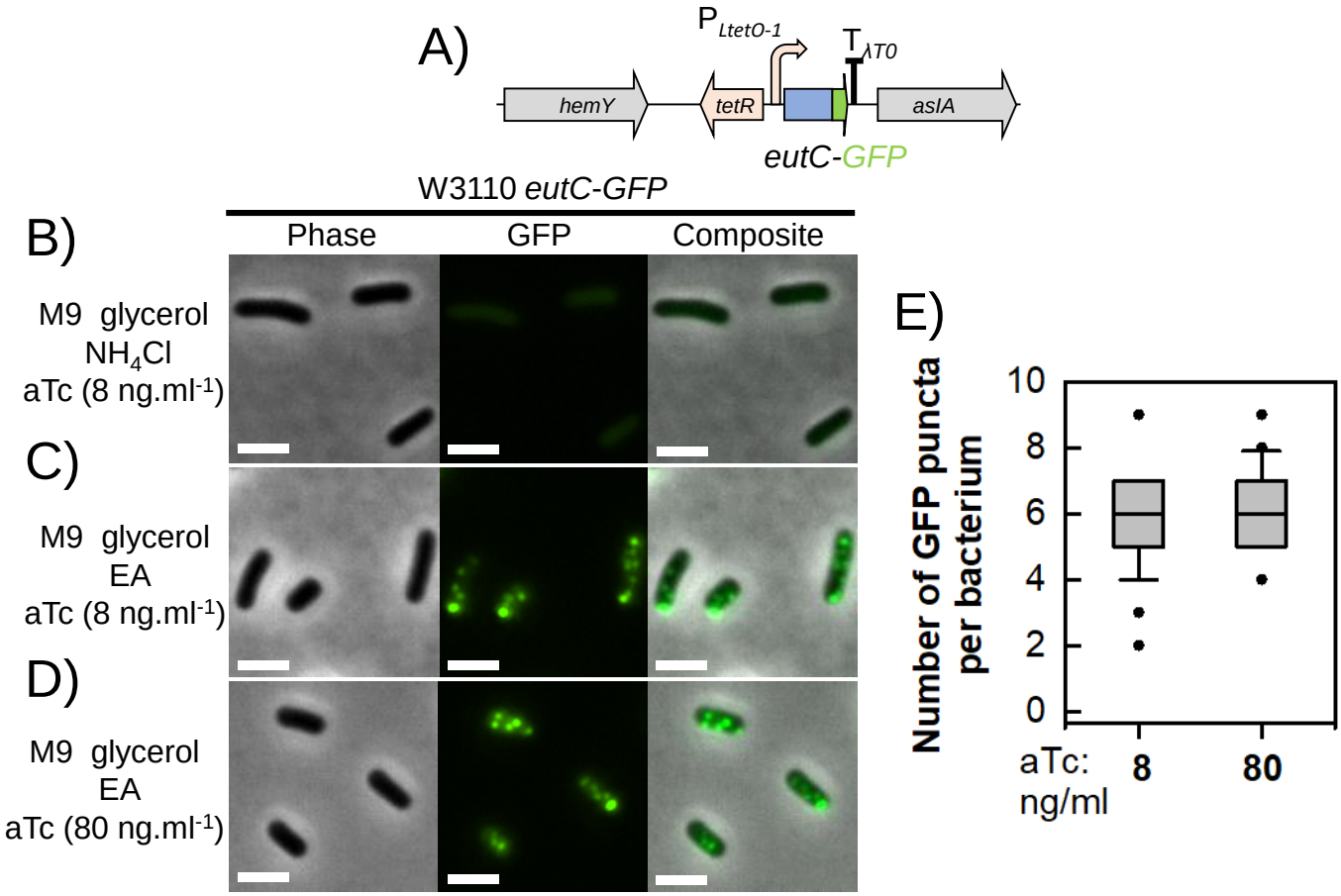

Figure 2. The chimeric protein EutC-GFP forms disctinct puncta in EA-containing medium. A) Schematic representation of the $P_{LtetO-1}$::*eutC-GFP* expression cassette. This construct was inserted at the *SS9* safe chromosomal locus in W3110 WT to produce W3110 *eutC-GFP*. B), C) and D) Representative micrographs showing phase contrast images, GFP fluorescence signals, and composite images from W3110 *eutC-GFP* grown in B) M9 glycerol NH_4Cl with 8 ng.ml^{-1} aTc, C) M9 glycerol EA vitamin B12 with 8 ng.ml^{-1} aTc and D) M9 glycerol EA vitamin B12 with 80 ng.ml^{-1} aTc. Scale bars indicate 2 µm. E) Box plots indicating the number of GFP puncta per bacterium (n = 30 analyzed cells) for cultures grown in M9 glycerol EA vitamin B12 with 8 ng.ml^{-1} or 80 ng.ml^{-1} aTc.

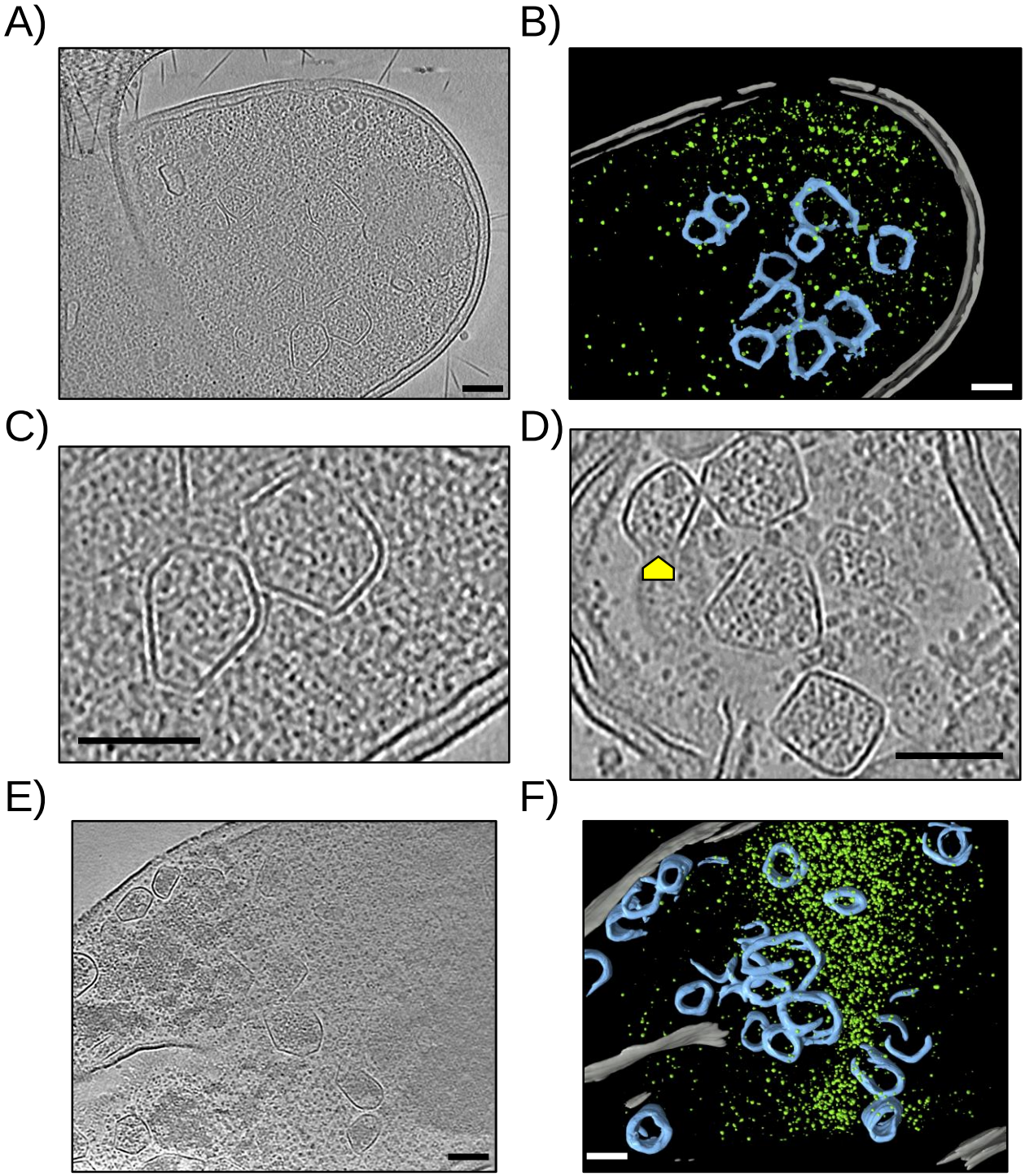

Figure 3. *E. coli* K-12 W3110 produces well-formed Eut BMCs. A) Representative electron cryotomogram slice of W3110 WT grown in M9 glycerol EA vitamin B12 and B) Associated 3D segmentation showing the cellular membranes in grey, the ribosomes in green, and the Eut BMCs in blue. C) and D) Expanded views of Eut BMCs illustrating their variety in size and shape. The yellow arrows in D) point towards possible cryoET (missing wedge) artefacts or partially assembled BMCs . E) Representative tomogram slice of W3110 Δeut pEut_WT grown in M9 glycerol EA IPTG and F) Associated segmentation. Scale bars indicate 100 nm.

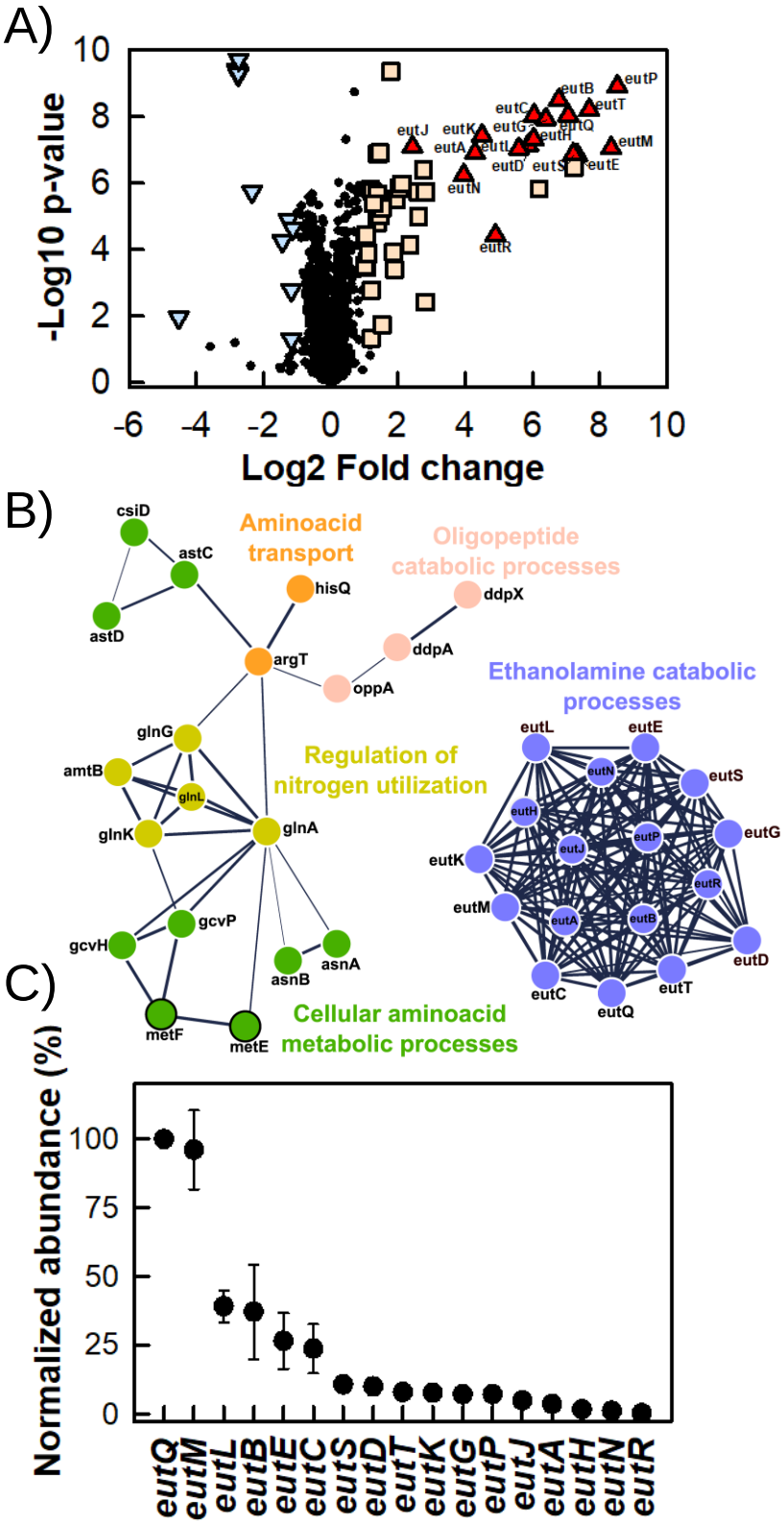

Figure 4. EA utilization requires minimal reorganization of the proteome. Cultures were grown aerobically in M9 glycerol EA vitamin B12 VS M9 glycerol NH_4Cl. Samples were collected for label-free quantitative mass spectrometry-based proteomics analyses. A) Volcano plot with Eut proteins (fold change > 2, $p < 0.05$) as red triangles, other upregulated proteins (fold change > 2, $p < 0.05$) as orange squares, downregulated proteins (fold change < -2, $p < 0.05$) as blue triangles, and unaffected proteins as black circles. B) Protein-protein interaction network as determined using STRING v11.5. Only selected upregulated (white outline) and downregulated (black outline) proteins are shown. Thicker lines indicate greater confidence in the considered protein-protein interactions. C) Normalized abundance (IBAQ score) of Eut proteins in M9 glycerol EA vitamin B12, using EutQ as the reference. Data shown are the mean of n = 4 biological replicates, bars correspond to standard deviations.

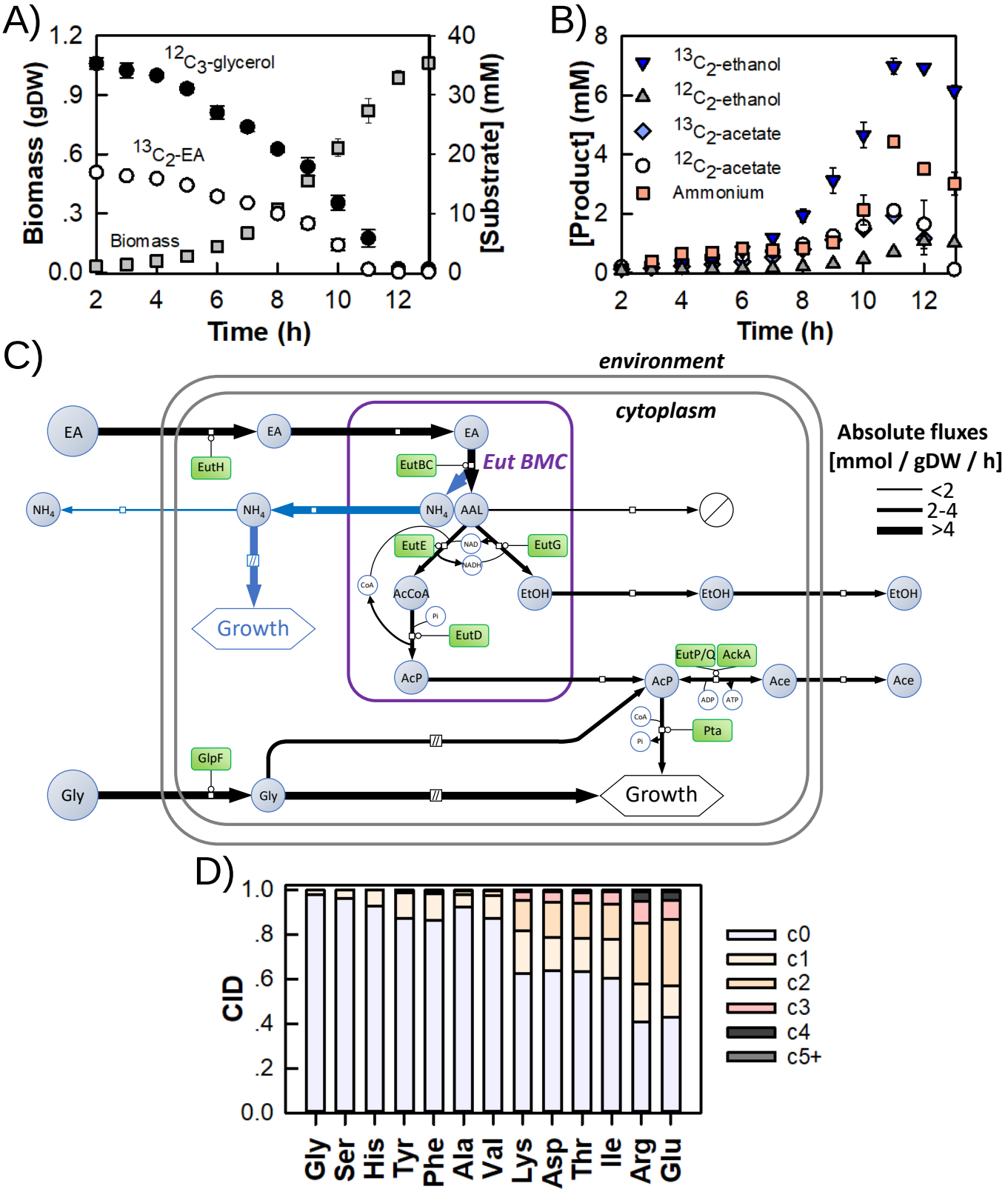

Figure 5. The *E. coli* K12 W3110 Eut BMCs turn EA into usable C and N sources. W3110 WT was grown aerobically in M9 medium containing $^{12}C_3$-glycerol and $^{13}C_2$-EA. A) Biomass accumulation (grams dry weight, gDW) and substrate consumption (mM); B) Product excretion. The substrates and products were quantified by ^{1}H-NMR. Data shown are the average of n = 3 biological replicates, bars correspond to standard deviations. C) Experimental and predicted fluxes through EA and glycerol metabolisms using an isotopic model. Absolute flux values are summarized in Table S4. Blue-filled circles indicate metabolites and green-filled rectangles indicate proteins. Unidentified sinks are indicated as barred white circles. D) Carbon isotopologue distribution (CID) within proteinogenic aminoacids from biomass samples harvested during exponential growth, showing the intracellular incorporation of ^{13}C derived from EA. AAL: acetaldehyde; AcCoA: acetyl-CoA; Ace: acetate; AcP: acetyl-phosphate; EtOH: ethanol; NH_4: ammonium.

Supplementary tables

Primer name	Sequence
F_bb1	TGAGCTAGCTGTCAAGGATCC
R_bb1	AAGTTAAAATAAGGCTAGTCCGTTAT
F_eutGgRNA	ATCCTTGACAGCTAGCTCAGTCCTAGGTATAATACTAGTCGGCACACCTTCGGTCAATG
R_eutGgRNA	ACTAGCCTTATTTTAACTTGCTATTTCTAGCTCTAAAACCATTGACCGAAGGTGTGCCG
F_bb2	CATAGTTAAGCCAGCCCCGA
R_bb2	TGTCGTGCCAGCTGCATTAAT
F_UA1	TTAATGCAGCTGGCACGACAGCGGCCGCAGCTGGCGGAGATCACCTTG
R_UA1	ACTCCCGCATCTTACCCTGAATATTCAGGGTAAGC
F_LA1	TCAGGGTAAGATGCGGGAGTGGGGGTGA
R_LA1	TCGGGGCTGGCTTAACTATGGCGGCCGCATTCACTGGCATCGCACCG
F_SS9gRNA	ATCCTTGACAGCTAGCTCAGTCCTAGGTATAATACTAGTTCTGGCGCAGTTGATATGTA
R_SS9gRNA	ACTAGCCTTATTTTAACTTGCTATTTCTAGCTCTAAAACTACATATCAACTGCGCCAGA
F_UA2	TTAATGCAGCTGGCACGACAGAATTCCCGACGTCCATCCAGCCC
F_UA2	GATATAATAAACCTGTTTGACATATCAACTGCGCCAGAGG
F_LA2	TCAAACAGGTTTATTATATCGCGTTGATTATTGATGC
R_LA2	TCGGGGCTGGCTTAACTATGGAATTCATAACCCGCCACAGTAGTTC
F_bb3	TACCAGTGGCGGCTAGTCTTGGACTCCTGTTG
R_bb3	TCGCCGCCTGTGCAGGATTAGCAGATGTGTG
F_eut1	TCTGCTAATCCTGCACAGGCGGCGACTCATG
R_eut1	GCGTAATCGCCCGCTGGGAGACTTTTTTCGCC
F_eut2	AAAGTCTCCCAGCGGGCGATTACGCTGCTCAAC
R_eut2	ATGCGCGCCCGCGCCAATCACCGTGGCGCGC
F_eut3	CACGGTGATTGGCGCGGGCGCGCATACCCT
R_eut3	AGTCCAAGACTAGCCGCCACTGGTACGCTGGG

Supplementary Table 1. Primers used in the present study.

Name	UniProt Id	Function	% Identity	% Similarity
eutJ	P77277	Chaperone of unknown function	88,9	93,6
eutN	P0AEJ8	Pentameric BMC shell protein	88	93
eutA	P76551	Ethanolamine ammonia-lyase reactivase	89,9	95,3
eutK	P76540	BMC shell protein	77,8	83,2
eutR	P36547	DNA-binding transcriptional activator	91,7	96,6
eutL	P76541	Trimeric BMC shell protein	94,1	97,7
eutD	P77218	Phosphate acetyltransferase	88,8	95,3
eutH	P76552	Ethanolamine permease	94,5	96,4
eutC	P19636	Ethanolamine-ammonia lyase small subunit	90,9	93,6
eutG	P76553	Alcohol dehydrogenase	80,5	85,8
eutB	P0AEJ6	Ethanolamine-ammonia lyase large subunit	98	99,3
eutQ	P76555	Probable acetate kinase	88	92,7
eutS	P63746	Hexameric BMC shell protein	94,6	99,1
eutE	P77445	Acetaldehyde dehydrogenase	93,8	97
eutT	P65643	Corrinoid adenosyltransferase	88,1	93,3
eutM	P41791	Hexameric BMC shell protein	95,9	96,9
eutP	P0A208	Probable acetate kinase	83,9	91,3

Supplementary Table 2. The predicted Eut proteins of *E. coli* K12 W3110. Sequence alignments were performed using EMBOSS-NEEDLE to determine the percentages of primary sequence identity and similarity with the Eut proteins of *Salmonella enterica* strain LT2.

Protein	Log2(fold-change)	-Log10(p-value)	Predicted function
eutP	8,53	8,91	Probable acetate kinase
eutM	8,34	7,05	Hexameric BMC shell protein
eutT	7,69	8,21	Corrinoid adenosyltransferase
eutE	7,33	6,85	Acetaldehyde dehydrogenase
amtB	7,23	6,47	Ammonium transporter, AMT family
eutS	7,22	6,87	Hexameric BMC shell protein
eutQ	7,07	8,05	Probable acetate kinase
eutB	6,79	8,50	Ethanolamine-ammonia lyase large subunit
eutG	6,41	7,93	Alcohol dehydrogenase
glnK	6,20	5,83	Nitrogen assimilation regulatory protein for GlnL, GlnE and AmtB
eutC	6,05	8,05	Ethanolamine-ammonia lyase small subunit
eutH	6,04	7,33	Ethanolamine permease
eutD	5,88	7,14	Phosphate acetyltransferase
eutL	5,59	7,03	Trimeric BMC shell protein
eutR	4,90	4,43	DNA-binding transcriptional activator
eutK	4,50	7,43	BMC shell protein
eutA	4,29	6,91	Ethanolamine ammonia-lyase reactivase
eutN	3,95	6,24	Pentameric BMC shell protein
priA	2,82	5,74	Primosomal protein n' (replication factor y)
ddpX	2,80	2,43	D-Ala-D-Ala dipeptidase, Zn-dependent
acrB	2,76	6,40	Multidrug efflux pumpRND permease
hrpA	2,61	5,00	ATP-dependent RNA helicase
ddpA	2,59	5,75	Putative d,d-dipeptide abc transporter periplasmic binding protein
eutJ	2,43	7,09	Putative chaperone
oppA	2,35	4,14	Oligopeptide abc transporter periplasmic binding protein
uxuA	2,12	5,97	D-mannonate dehydratase
guaD	2,03	5,85	Guanine deaminase
ampC	1,95	5,50	β-lactamase
cbl	1,88	3,42	DNA-binding transcriptional activator Cbl
ybiO	1,87	3,93	Mechanosensitive channel
gcvP	1,79	9,36	Glycine decarboxylase
glnL	1,53	5,27	Two-component system, ntrc family
yqjH	1,53	1,74	NADPH-dependent ferric chelate reductase
cycA	1,46	5,02	D-serine/alanine/glycine/:H^+symporter
rsmA	1,45	6,92	rRNA dimethyltransferase
astD	1,40	6,87	Succinylglutamate-semialdehyde dehydrogenase
glnA	1,40	5,67	Glutamine synthetase
astC	1,38	4,82	Succinylornithine transaminase
glnG	1,35	5,37	Two-component system, ntrc family
rnpA	1,27	5,38	Ribonuclease P protein
asnB	1,25	5,73	Asparagine synthase (glutamine-hydrolysing)
hisQ	1,21	2,78	Lysine/arginine/ornithine ABC transporter, membrane subunit
gcvH	1,20	1,33	Glycine cleavage system H protein
argT	1,19	5,83	Lysine/arginine/ornithine ABC transporter, periplasmic binding protein
ygiQ	1,11	3,90	Protein of unknown function
dgcM	1,05	4,45	Diguanylate cyclase
asnA	1,05	3,46	Aspartate-ammonia ligase
fbp	1,01	3,53	Fructose-1,6-bisphosphatase class 1
yciF	-1,13	4,64	Putative rubrerythrin/ferritin-like metal-binding protein
glaH	-1,17	2,79	Glutarate dioxygenase
ybjP	-1,18	1,30	DUF3828 domain-containing lipoprotein
metF	-1,26	4,90	Methylenetetrahydrofolate reductase
phoA	-1,44	4,26	Alkaline phosphatase
lldD	-2,34	5,74	L-lactate dehydrogenase
metE	-2,74	9,72	Cobalamin-independent homocysteine transmethylase
nhaA	-4,52	1,96	Na^+:H^+ antiporter

Supplementary Table 3. List of the *E. coli* K12 W3110 WT proteins that were differiantially accumulated in M9 glycerol EA vit B12 compared to M9 glycerol NH_4Cl (|Log2(fold-change)|>1 and -Log10(p-value)>1,3). The annotated functions as indicated on STRING v11.5 are also reported.

Reaction	Description	Localization	Value
Experimentally determined values			
μ	Growth rate (h^{-1})	NA	0.37 ± 0.01
$q_{S)Glycerol}$	Glycerol uptake from extracellular medium	Extracellular	13.68 ± 0.15
$q_{S)Ethanolamine}$	Ethanolamine uptake from extracellular medium	Extracellular	7.04 ± 0.23
$q_{P)Ethanol}$	Ethanol excretion into extracellular medium	Cytosol	2.67 ± 0.11
$q_{P)Acetate}$	Acetate excretion into extracellular medium	Cytosol	1.64 ± 0.09
$q_{P)NH4}$	Ammonium excretion into extracellular medium	Extracellular	0.86 ± 0.21
Predicted values for ethanolamine-derived acetaldehyde metabolism			
v_{EutBC}	EAL	BMC	7.04 ± 0.23
$v_{eBMC)Acetaldehyde}$	Acetaldehyde leakage from the Eut BMCs	BMC	2.67 ± 0.11
v_{EutG}	Acetaldehyde to ethanol conversion (NAD^+-dependent)	BMC	2.67 ± 0.11
$v_{eBMC)Ethanol}$	Ethanol diffusion out of the BMC	BMC	2.67 ± 0.11
v_{EutE}	Acetaldehyde to acetyl-CoA conversion (NADH-dependent)	BMC	2.67 ± 0.11
v_{EutD}	Acetyl-CoA to acetyl-P conversion	BMC	2.67 ± 0.11
$v_{eBMC)Acetyl\text{-}P}$	Acetyl-P diffusion out of the BMC	BMC	2.67 ± 0.11
Predicted values for glycerol metabolism			
$V_{gly)biomass}$	Biomass production from glycerol	Cytosol	11.17 ± 0.20
$V_{gly)glycolysis}$	Acetyl-P production from glycerol	Cytosol	2.51 ± 0.06
Predicted values for cytosolic acetyl-P metabolism			
$v_{EutP,\ EutQ,\ AckA}$	Acetyl-P to acetate conversion	Cytosol	1.64 ± 0.09
v_{Pta}	Acetyl-P to acetyl-CoA (to biomass) conversion	Cytosol	3.54 ± 0.14
Predicted values for ethanolamine-derived ammonium metabolism			
$v_{eBMC)NH4}$	Ammonium diffusion out of the BMC	BMC	7.04 ± 0.23
$v_{NH4)biomass}$	Biomass production from ammonium	Cytosol	6.18 ± 0.08

Table S4. Growth parameters of *E. coli* K12 W3110 WT cultivated aerobically in M9 medium containing $^{12}C_2$-glycerol, $^{13}C_2$-EA and vit B12. The experimentally determined substrate uptake (q_S) and product excretion (q_P) rates are expressed in mmol.(gDW.h)$^{-1}$. Intracellular flux values (v) determined using the isotopic model are also expressed in mmol.(gDW.h)$^{-1}$. DW: dry weight; NA: not appliable. Data is the average of n=3 independent replicates, errors indicate SD.

Supplementary figures

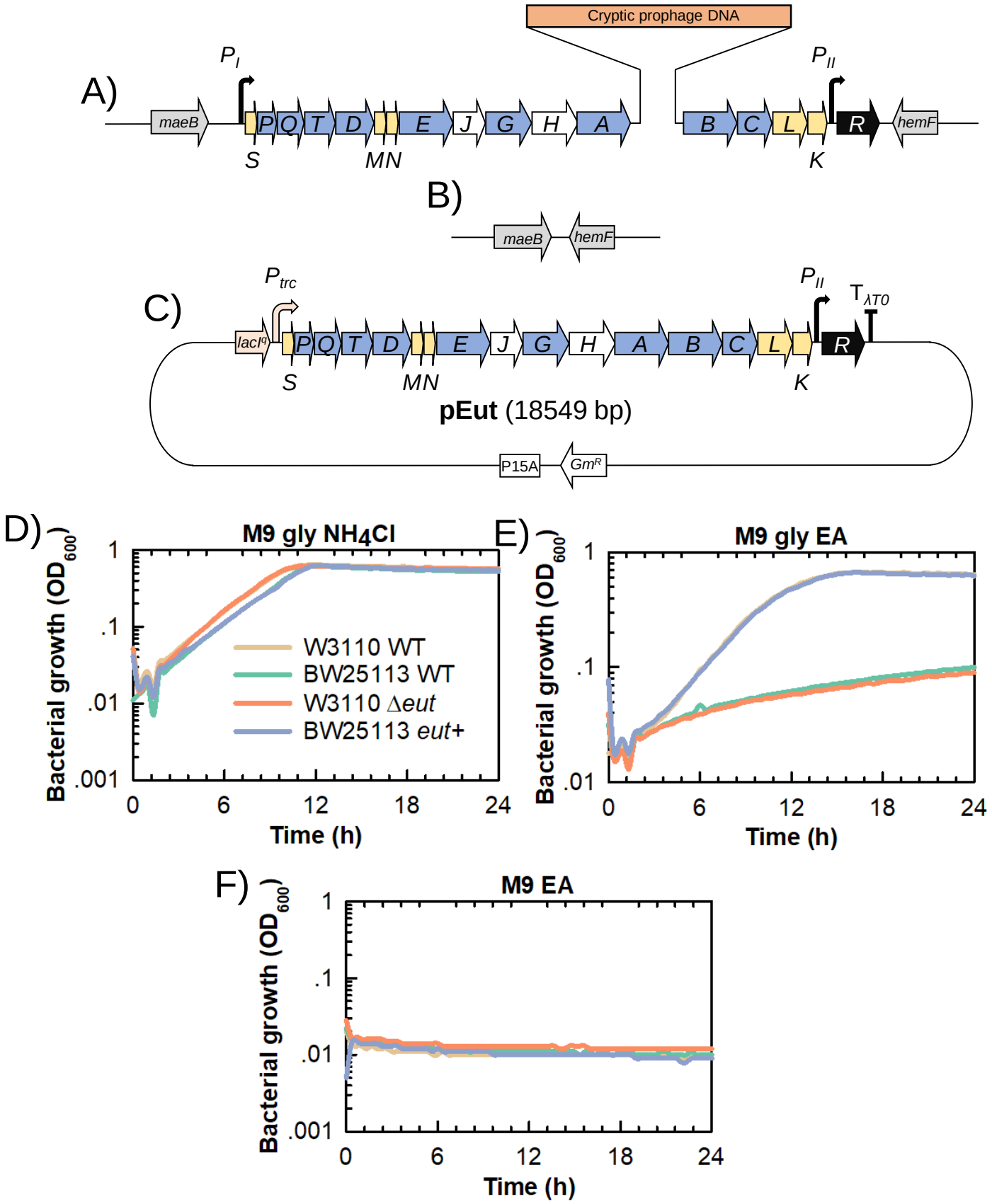

Figure S1. Capacity to utilize EA as a N source in *Escherichia coli* K12 and mutant derivatives. Schematic representation of the *eut* operon in A) the chromosome of BW25113 WT where it harbors a 6,9 kb prophage DNA insertion downstream *eutA*, B) the chromosome of W3110 *Δeut* where the entire operon was scarlessly removed by genome editing and C) the pEut plasmid where the *eut* operon from W3110 WT was cloned into pSEVA661 under control of the IPTG-inducible P_{trc} promoter. The BW25113 *eut+* mutant was generated by scarlessly removing the prophage DNA insertion through genome editing, thus reconstituting an uninterrupted *eut* operon (yielding the same *eut* operon as in W3110 WT). D) to F) Plate reader measurement of optical density at 600 nm over time. The strains were grown in D) M9 derivative with glycerol as the C source and NH_4Cl as the N source; E) M9 derivative with glycerol as the C source and EA as the sole N source, including also vitamin B12; F) M9 derivative with EA (160 mM) as the C and N source, including also 200 nM vitamin B12. Data shows a representative experiment out of at least n = 3 independent replicates.

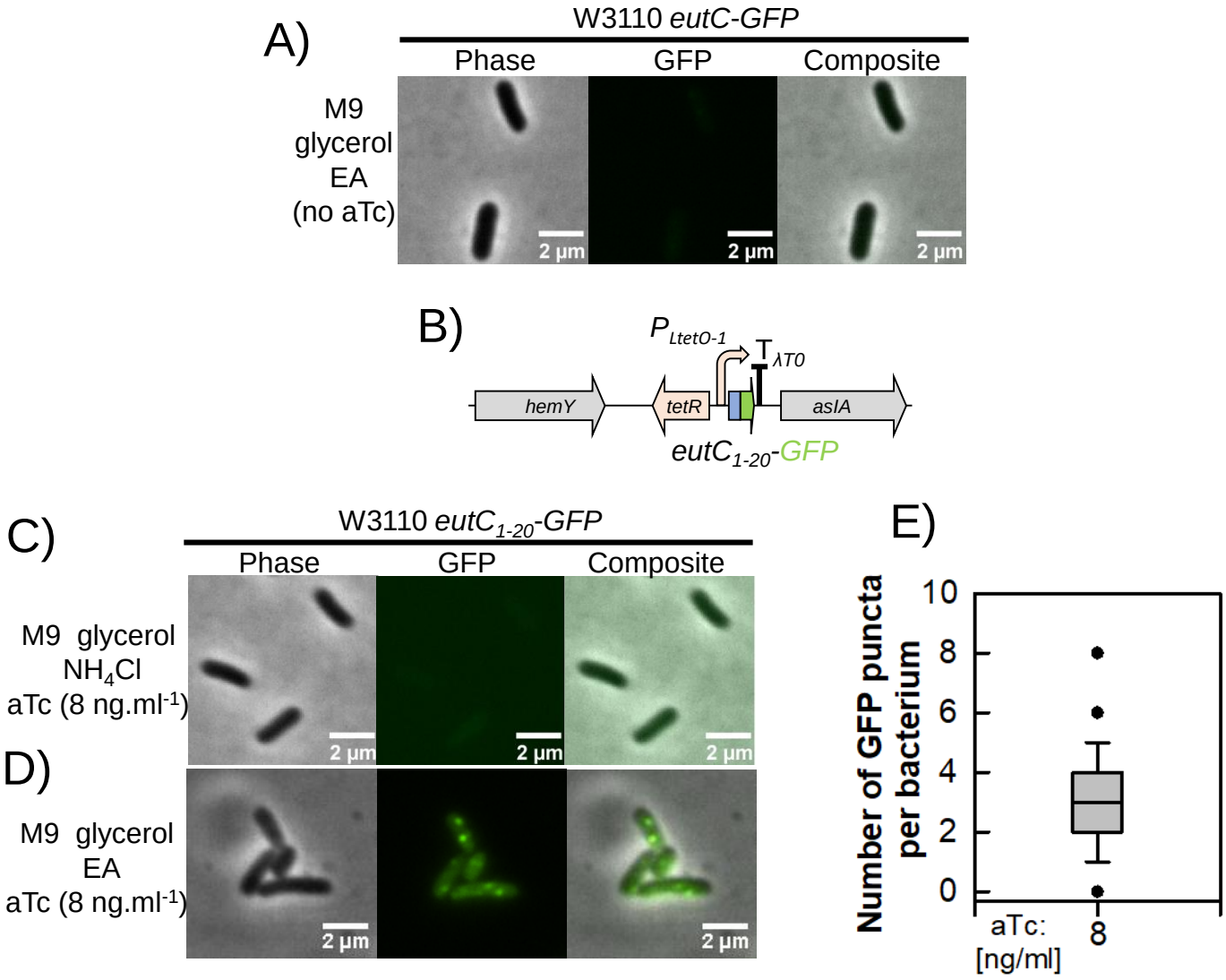

Figure S2. Epifluorescence microscopy to determine the EutC-GFP and EutC$_{1-20}$-GFP subcellular localization. A) Representative micrograph showing a phase contrast image, GFP fluorescence signal as well as a composite image from W3110 *eutC-GFP* grown in M9 glycerol EA vit B12 without any aTc added. B) Schematic representation of the P$_{LtetO-1}$::eutC$_{1-20}$-GFP expression cassette. This construct was inserted at the SS9 safe locus site in W3110 WT to yield W3110 *eutC$_{1-20}$-GFP*. C) and D) Representative micrographs showing phase contrast images, GFP fluorescence signal as well as composite images from W3110 *eutC$_{1-20}$-GFP* grown in C) M9 glycerol NH_4Cl with 8 ng.ml^{-1} aTc and D) M9 glycerol EA vit B12 with 8 ng.ml^{-1} aTc. E) Box plot indicating the number of GFP puncta per bacterium out of n = 30 individual cells for cultures grown in M9 glycerol EA vit B12 with 8 ng.ml^{-1} aTc.

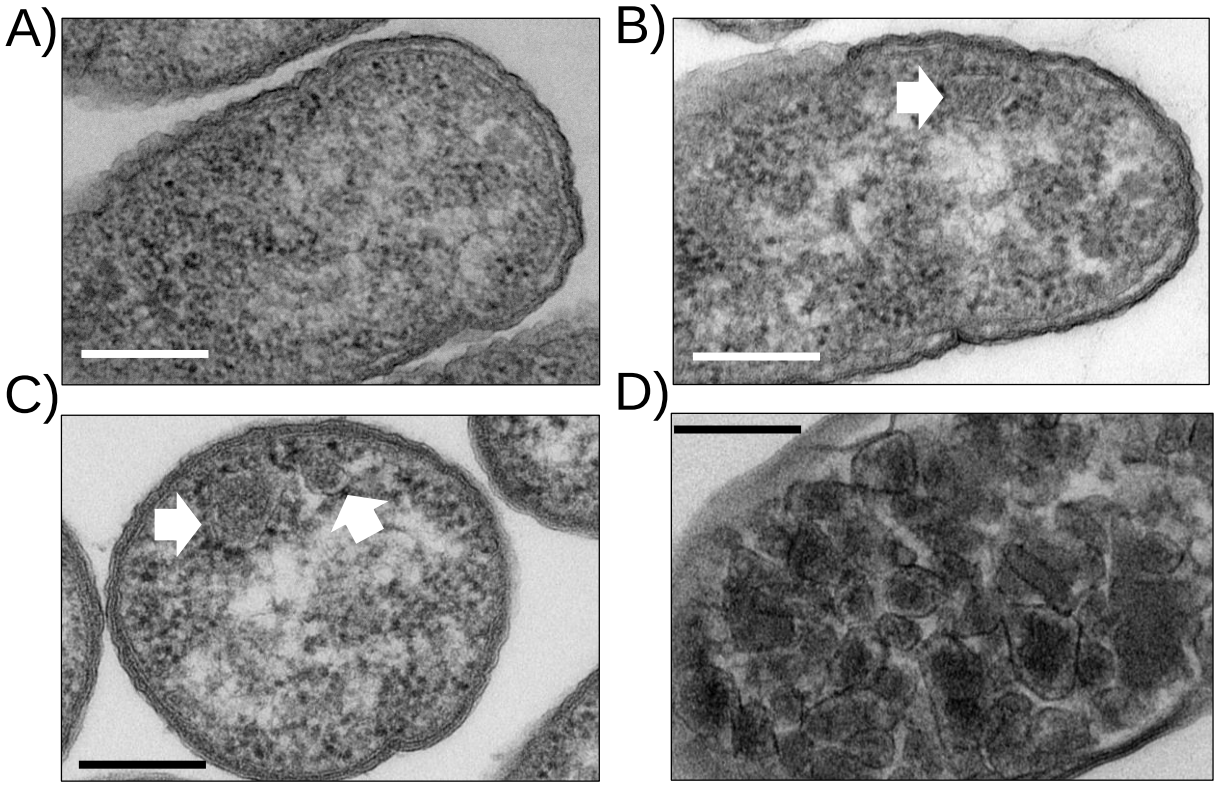

Figure S3. Observation of the *Escherichia coli* K12 W3110 Eut BMCs by TEM. A) W3110 WT in M9 glycerol NH_4Cl; B) W3110 WT in M9 glycerol EA vit B12; C) W3110 WT in LB EA vit B12 and D) W3110 Δeut pEut_WT in LB 20 µM IPTG. The filled white arrows indicate Eut BMCs in B and C. Scale bars show 200 nm.

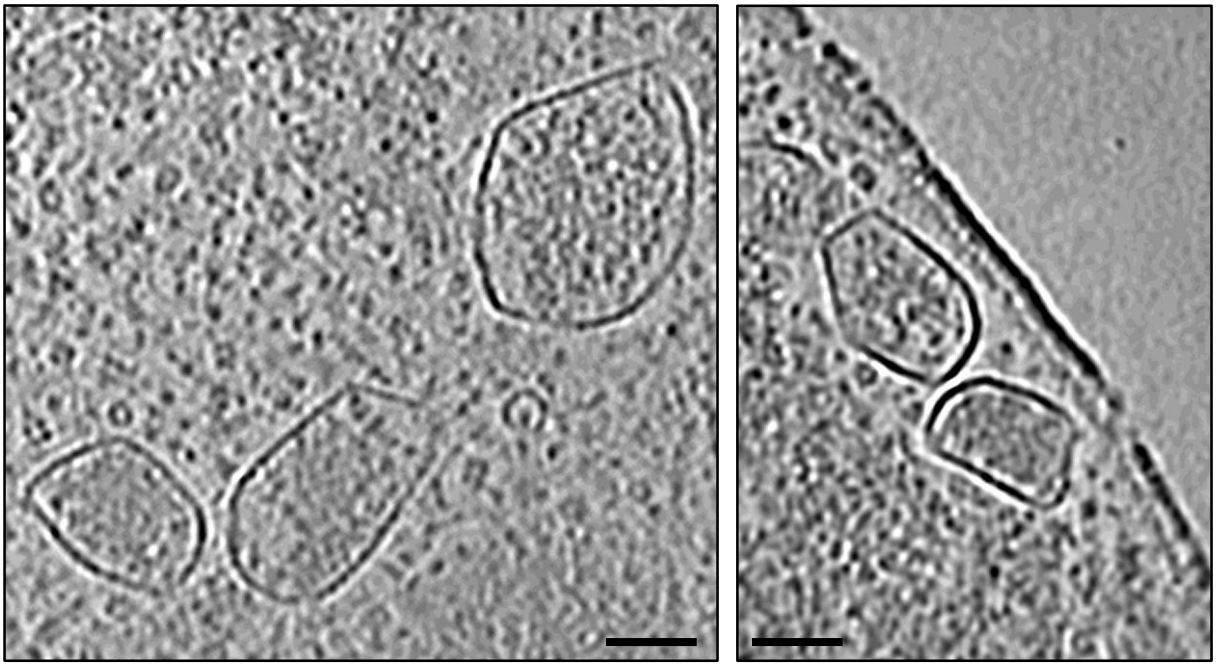

Figure S4. CryoET observation of the Eut BMCs formed by W3110 Δ*eut* pEut. The *eut* overexpressor strain was grown in M9 glycerol EA with 20 µM IPTG. Representative electron cryotomogram slices are shown. The scale bars indicate 50 nm.

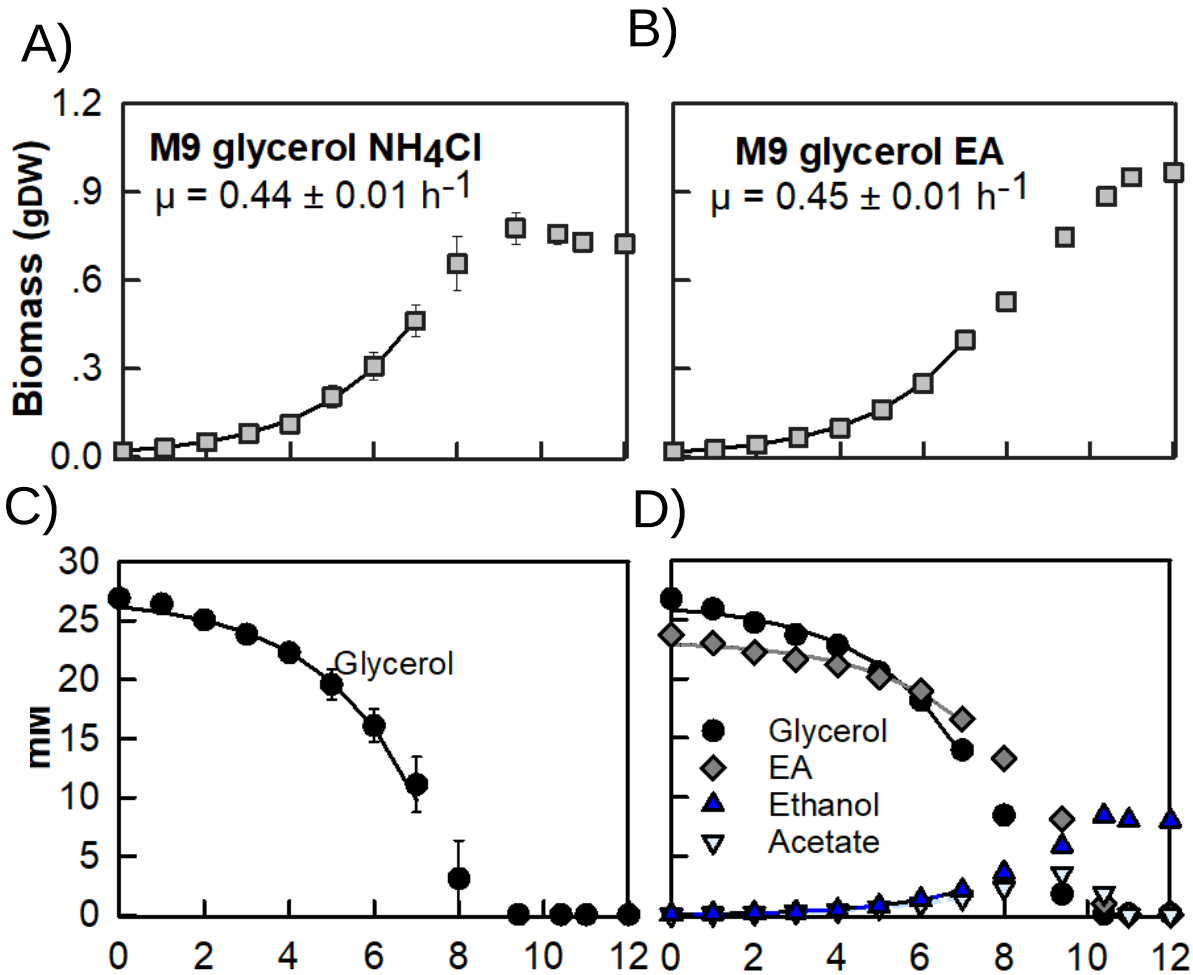

Figure S5. Physiological characterization of *Escherichia coli* K12 W3110 WT grown in M9 glycerol containing NH_4Cl or EA as the sole N source. Cultures were grown aerobically in A) and C) M9 glycerol (30 mM) NH_4Cl (25 mM) or B) and D) M9 glycerol (30 mM) EA (25 mM) vit B12 (200 nM). A) and B) Biomass accumulation (grams dry weight, gDW); C) and D) Exometabolome profiling by ^{1}H-NMR. Data is the average of n = 3 biological replicates, bars show SD. The solid lines are the best fits obtained with PhysioFit.

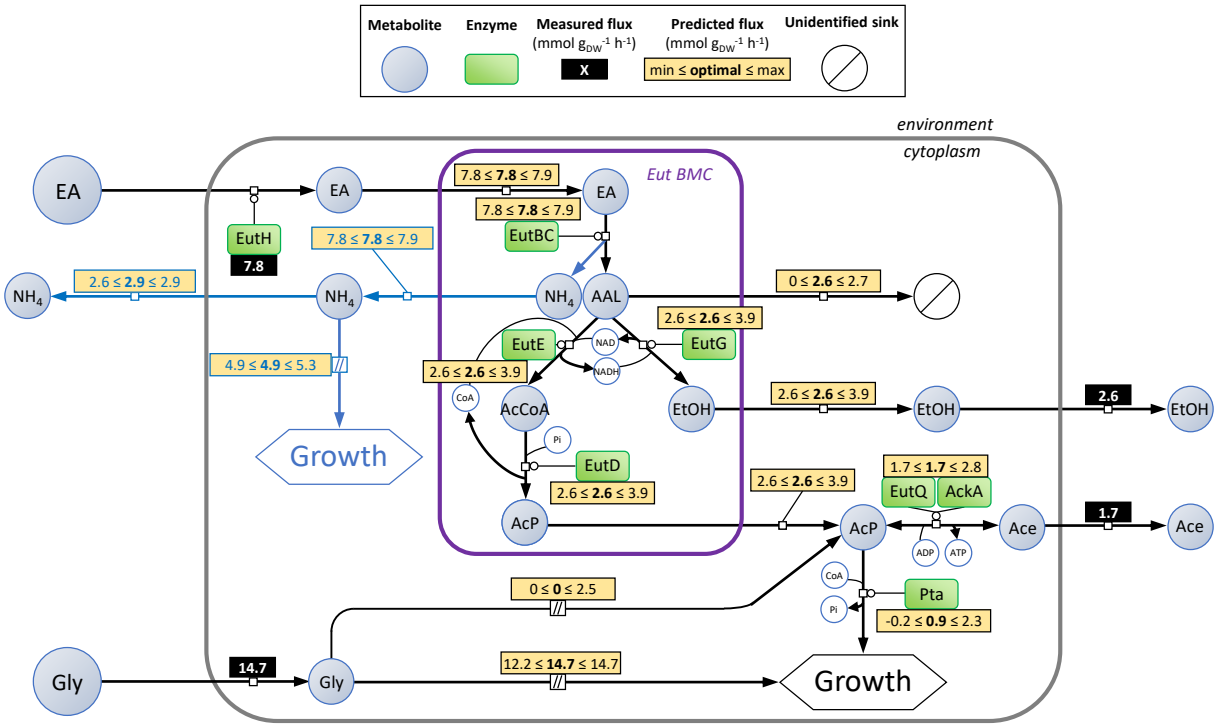

Figure S6. FBA/FVA analysis of EA metabolism in *E. coli* K-12 W3110. Black rectangles indicate the experimentally determined exchange fluxes for W3110 WT grown in M9 glycerol (30 mM) EA (25 mM) (data from Fig.S5). Yellow rectangles report the predicted fluxes. The BMC-associated fluxes were deduced assuming that NADH and CoA-SH are recycled internally while ATP is recycled within the cytosol. We also assumed that acetate and ethanol were produced from the BMCs. The non-constrained fluxes were simulated by flux balance analysis (optimal value: bold font) combined with flux variability analysis (to determine possible value ranges while maintaining 99% of the fitness). Our model aimed at maximizing ATP production while the growth rate was set to 0.45 h^{-1} to match the experimental data. Flux values are given in mmol.g_{DW}^{-1}.h^{-1}. AAL: acetaldehyde; AcCoA: acetyl-CoA; AcP: acetyl-phosphate; EtOH: ethanol; Gly: glycerol; NH_4: ammonium.

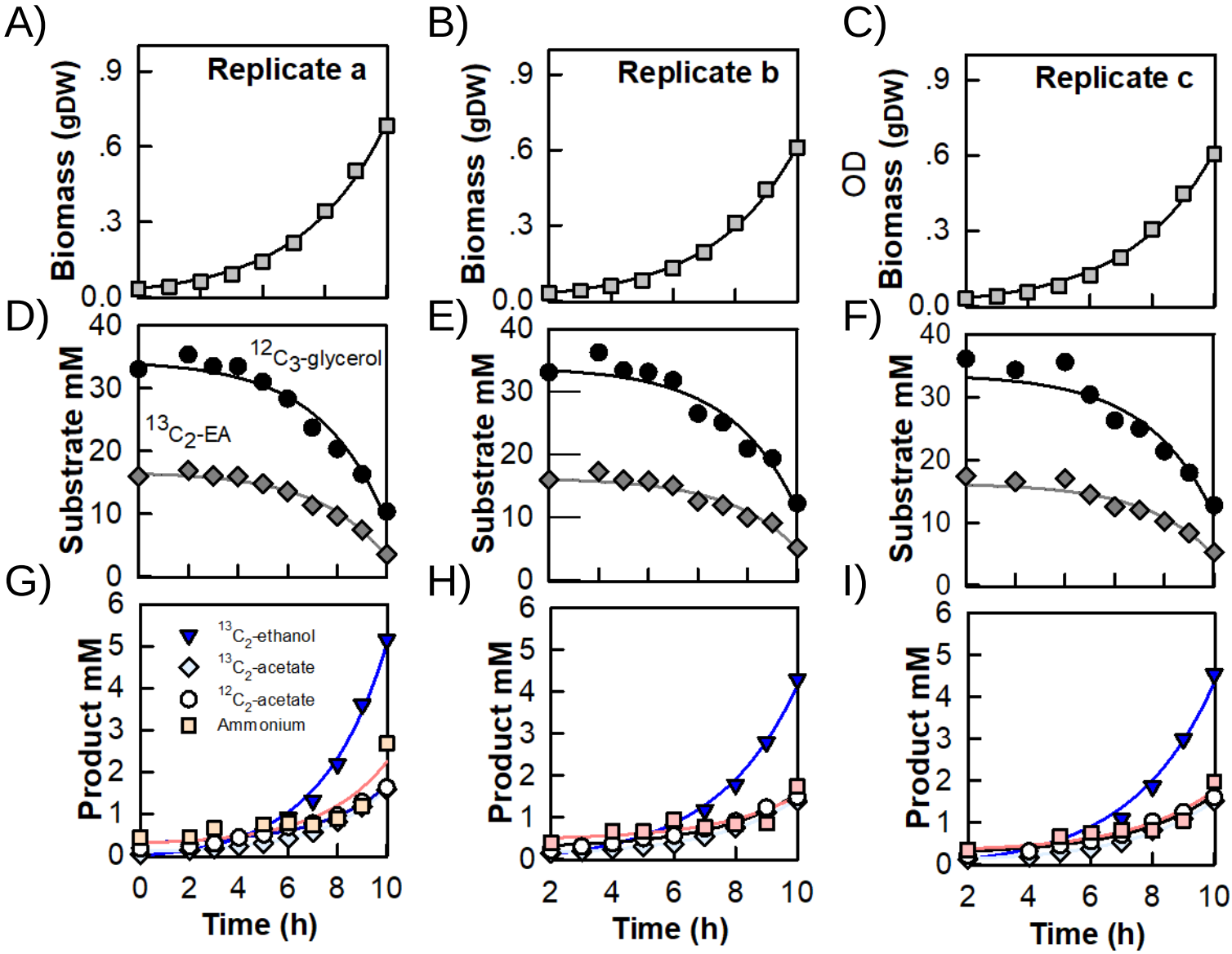

Figure S7. The dynamic isotopic model fits the experimental data satisfactorily. W3110 WT cultures (3 biological replicates named a, b and c) were grown aerobically in M9 medium containing $^{12}C_3$-glycerol and $^{13}C_2$-EA. A), B) and C) Biomass accumulation (grams dry weight, gDW) in biological replicates a, b and c. Exometabolome composition was determined by ^{1}H-NMR. D), E) and F) $^{12}C_3$-glycerol and $^{13}C_2$-EA uptake in biological replicates a, b and c. G), H) and I) $^{13}C_2$-EtOH, $^{13}C_2$-acetate, $^{12}C_2$-acetate and ammonium production in biological replicates a, b and c. Solid lines show the best fits with our dynamic isotopic model. The experimental data from all 3 replicates were averaged to produce Figure 5.

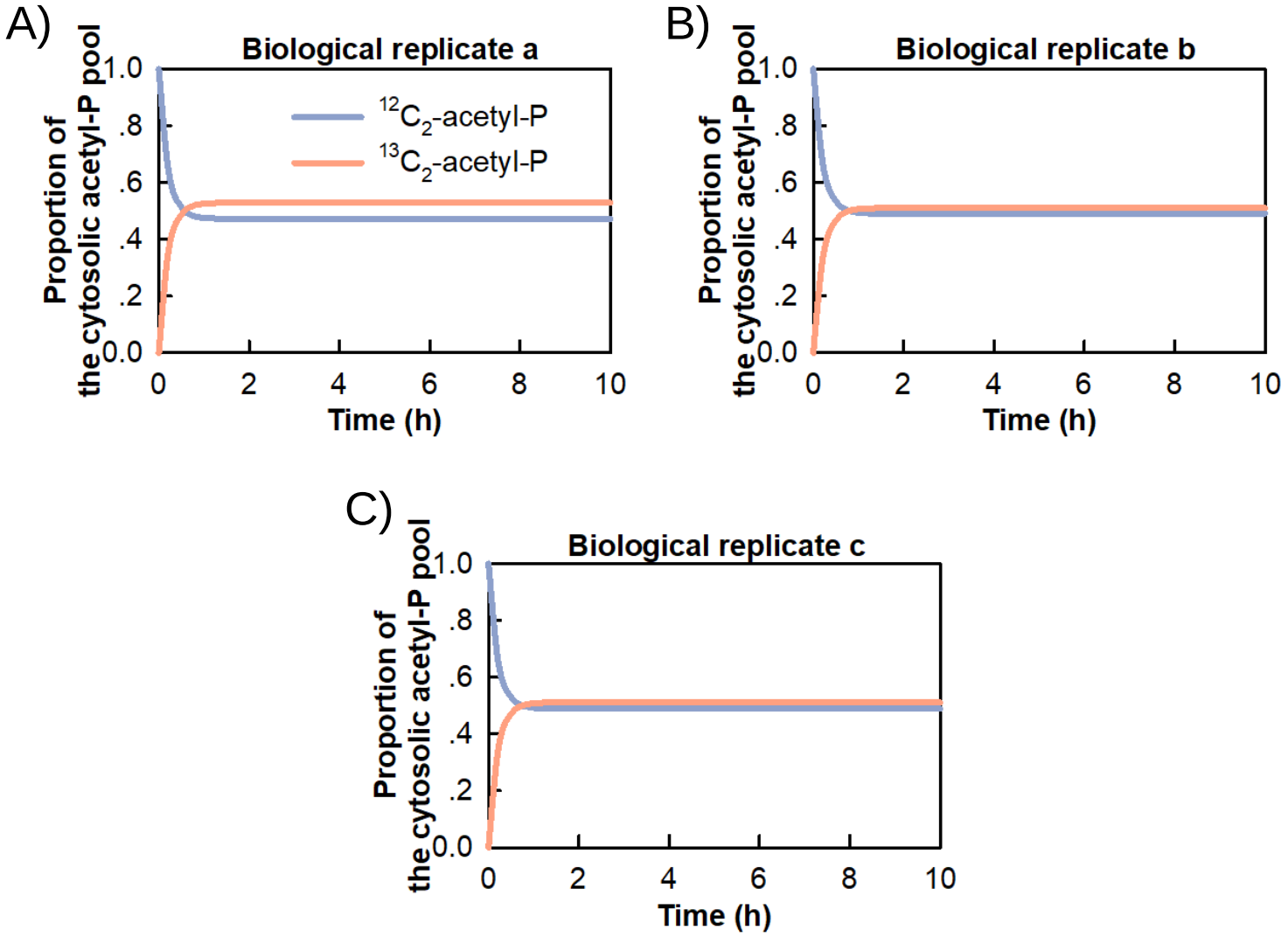

Figure S8. Predicted evolution of the cytosolic acetyl-P pool isotopic composition. The isotopic model was used to fit data from Fig.5. The predicted proportion of cytosolic $^{12}C_2$-acetyl-P (derived from glycerol) VS $^{13}C_2$-acetatyl-P (derived from EA) over time is shown for each biological replicate (A to C).